Instability of Frontal Waves

ISIDORO ORLANSKI

Massachusetts Institute of Technology, Cambridge[1]

(Manuscript received 11 September 1967)

ABSTRACT

The stability of the classical Norwegian polar front model is investigated, using a numerical technique to supplement the more precise conclusions which are possible in the limiting cases of zero density difference or zero wavenumber. The feasibility of the numerical technique depends on a careful formulation of boundary conditions at the limits of the frontal zone. The numerical results cover the region of Rossby number (Ro)$\leq$3 and Richardson number (Ri)$\leq$5, but their interpretation is unclear at Ri$>$2 and Ro$>$1. Unstable waves exist at all wavelengths; Rayleigh shear instability at small Ri, Helmholtz shear instability at large Ro and small Ri, shear instability and geostrophic baroclinic instability simultaneously at small Ro and Ri$>$2, and a combination of geostrophic and Helmholtz instability when Ri$>$2 and Ro$<$1 (but not too small). The previous conclusion of Kotschin that this frontal model is stable for Ri$<$2 is therefore incorrect.

1. Introduction

Due to the difficulties involved in studying the general circulation of the atmosphere as a whole, investigators have studied each atmospheric phenomenon separately. Examples are: baroclinic instability (Charney, 1947), conversion of energy in the mean flow and perturbations (Fjørtoft, 1951), transformation of energy of baroclinic waves in a two-layer model (Phillips, 1954), and formation and development of atmospheric fronts (Bjerknes, 1919; Solberg, 1928; Kotschin, 1932). In order to give quantitative estimates of the processes involved, simplified mathematical models are frequently used in these studies.

One approach to the formulation of a unified theory of the basic processes involved in these phenomena would be to try to identify the energy sources which support them: the modifications produced in the mean flow by the perturbations, and the energy transports to different latitudes which may act as energy sources for new types of instabilities. From this general point of view, the problem of fronts plays an important role, because large transformations of energy as well as intense local effects are involved.

The theory of fronts originated with the Norwegian school, when in 1920, V. Bjerknes suggested that the extratropical cyclone is an amplifying wave motion which develops on the sloping frontal surface as a result of some kind of instability. Solberg (1928) investigated theoretically a system consisting of two statically stable, barotropic layers of different density moving zonally at different speeds. To avoid the singularity associated with the intersection of the frontal interface with the ground, he introduced two rigid bounding planes which were not horizontal but were parallel to the undisturbed sloping frontal surface. With this constraint he found that two types of amplifying waves were possible, one at short wavelengths and one at wavelengths of the order of 2000 km. The latter wavelength corresponds to the horizontal scale of extratropical cyclones.

Bjerknes and Godske (1936) gave a physical interpretation of the long unstable waves found by Solberg, attributing them to shearing instability. This interpretation was later questioned by Høiland (1948), who showed that long unstable waves of the same nature as those found by Solberg may appear as a result of an interaction between the shear and the internal static stability of the two layers. In this way the long unstable waves would not be a simple manifestation of shearing instability, but the result of a more complex process. From an energetic point of view Solberg's model gives a contribution from both the mean potential and kinetic energy to the growing perturbation energy. On the other hand, it is known that the long-wave perturbations in the atmospheric westerlies on the average lose energy to the kinetic energy of the mean flow while gaining energy from the potential energy of the mean flow. Theoretical analyses by Charney (1951) and Pedlosky (1964) have shown this process to occur in a quasi-geostrophic model in which the basic current varies with latitude and height.

The problem of frontal waves was also studied by Kotschin (1932), who considered two incompressible homogeneous fluids with a shear and a slight density difference, bounded above and below by two rigid horizontal planes. He found a stability criterion relating the frontal slope with the wave number. Eliasen (1960) studied a similar model but with the simplification of a vertical wall at the northern boundary, so that the

[1] Present affiliation; Geophysical Fluid Dynamics Laboratory, ESSA, Washington, D. C.

frontal surface did not intersect the rigid top surface. He extended Kotschin's results by computing the unstable modes for particular values of the frontal slope.

As the density difference in these models is reduced, the sloping front becomes more vertical. Because of the shear, however, one would still expect to find unstable solutions in this limit. Nevertheless, Kotschin's stability criterion does not admit this possibility. (Eliasen also does not find this kind of instability. But this may be due to his introduction of the side wall, a restriction which reduces the lateral extent of the frontal zone as the slope steepens.)

The idea of the existence of a second kind of frontal instability distinct from that found by Kotschin and Eliasen, the desirability of understanding the complete features of these two different instabilities in the whole spectrum, and the location in spectral space as a function of Richardson (Ri) and Rossby (Ro) numbers of the regions of pure baroclinic, pure barotropic, and baroclinic-barotropic instabilities,[2] led to the investigation which forms the basis for the present paper. The frontal model is the same as that used by Kotschin.

Following a formulation of the steady state and linearized perturbation equations in Sections 2 and 3, Section 4 is devoted to the limiting case of pure shear instability. In this case the densities are identical and the frontal surface is vertical. Unstable waves exist (Rayleigh instability), together with neutral inertial waves. This situation exists when the Richardson number

$$\mathrm{Ri}=\frac{gH(\rho_1-\rho_2)}{\left(\frac{\rho_1+\rho_2}{2}\right)(U_2-U_1)^2}$$

vanishes. (H is the total depth, and ρ_1 and ρ_2, U_1 and U_2 are the densities and undisturbed basic currents in the two fluid layers.) A study of long waves, in which the x wave wavenumber k vanishes, but the phase velocity is finite, is presented in Section 5. This is a slight extension of Kotschin's work and demonstrates that new instabilities appear as Ri becomes successively greater than 2, 6, 12, etc. Kotschin concluded from his analysis of this limiting case that the frontal surface was stable if $\mathrm{Ri}<2$. The non-dimensional statement that $k=0$ is expressed by the vanishing of the Rossby number,

$$\mathrm{Ro}=\frac{(U_2-U_1)k}{2f},$$

where f is the Coriolis parameter. It is shown that these instabilities are similar to the quasi-geostrophic baroclinic instabilities found by Charney (1947) and Eady (1949). In Section 6 a brief analysis is made of the location, as a function of Ro and Ri, of frequencies corresponding to neutral waves which move with the mean flow, $(U_2+U_1)/2$. Section 7 contains the major contribution of this paper and consists of a numerical determination of the unstable wave eigenfrequencies in the region $0\leq\mathrm{Ro}\leq 3$, $0\leq\mathrm{Ri}\leq 5$. In addition to the two instability types mentioned above, it is found that Helmholtz (hydrostatic, with shear and gravitational stability) instabilities exist at large Ro, while at $\mathrm{Ro}<1$ the shear instability and the geostrophic instability coalesce into a mixed type. The net result is that unstable waves exist at all values of k. In particular, Kotschin's conclusion that the frontal surface is stable if $\mathrm{Ri}<2$, is incorrect. Furthermore, the differing simplified interpretations by Bjerknes-Godske and by Høiland of the Solberg waves may therefore both be correct.

The paper concludes with a discussion of the kinematics and energetics of the waves, with primary emphasis on the mixed instability waves at $\mathrm{Ro}<1$ and $\mathrm{Ri}>2$. At small Ro these waves receive energy from the potential energy of the mean flow, but return some to the kinetic energy of the mean flow. As Ro becomes closer to 1, however, they receive energy from both the mean flow potential energy and kinetic energy, partaking thereby of the characteristics of the geostrophic instability and Helmholtz instability.

Stone (1966) has analyzed the instabilities present in the continuously stratified model of Eady in the absence of lateral boundaries to the basic current. Several of his results, although they apply to a model with continuous density stratification, and with different geometry and boundary constraints than the classical frontal model used here, carry over to the results of the present paper —geostrophic instabilities are dominant when Ri is large, and Helmholtz instabilities dominate when Ri is small.

2. The unperturbed steady state front

We consider two layers of incompressible homogeneous fluid in a rotating coordinate system with constant Coriolis parameter f. The motion in each layer is hydrostatic and independent of the vertical coordinate z, and the two fluids are bounded above and below by rigid horizontal planes at $z=0$ and $z=H$. The interface between the layers at $z=h(0\leq h\leq H)$ is

$$z=h(x,y,t)=\text{interface height.} \tag{2.1}$$

Let $\mathbf{k}$ be a vertical unit vector, and ∇ the horizontal gradient operator. Let $\mathbf{v}_j=(u_j,v_j)$, with $j=1$ and 2, represent the horizontal velocity in the lower ($j=1$) layer and upper ($j=2$) layer. Pressures p_1 and p_2 are given at $z=0$ and $z=H$, respectively. The equations governing this model, which satisfy the dynamic and

[2] The adjectives *barotropic* and *baroclinic*, when used in this paper, refer to instabilities whose energy source is the kinetic energy or potential energy of the mean flow. *Barotropic* in this sense does not necessarily imply flow patterns which are invariant with height.

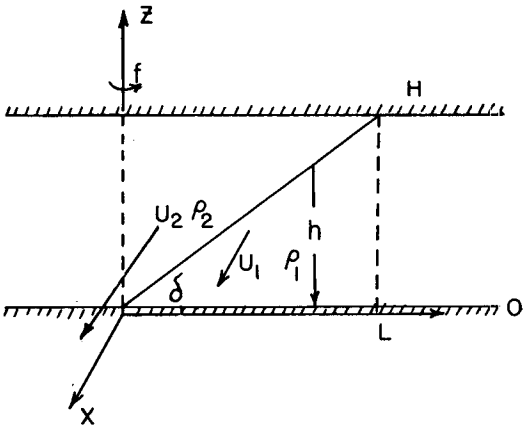

FIG. 1. Frontal surface model.

kinematic conditions at $z=0$, h and H are as follows:

$$\left[\frac{\partial}{\partial t}+(\mathbf{v}_j\cdot\nabla)+f\mathbf{k}\times\right]\mathbf{v}_j=-\frac{1}{\rho_j}\nabla p_j, \tag{2.2}$$

$$p_1=p_2+(\rho_1-\rho_2)gh+\rho_2 gH, \tag{2.3}$$

$$\frac{\partial h}{\partial t}=-\nabla\cdot h\mathbf{v}_1=\nabla\cdot(H-h)\mathbf{v}_2. \tag{2.4}$$

The density ρ_1 of the lower layer is not less than its value ρ_2 of the upper layer.

The basic state consists of a uniform velocity U_j in the positive x direction in each layer. For a steady solution of this nature, (2.2)–(2.4) require that

$$\tan\delta=\frac{d\bar{h}}{dy}=\frac{f(\rho_2U_2-\rho_1U_1)}{g(\rho_1-\rho_2)}, \tag{2.5}$$

$$\frac{d}{dy}(\bar{p}_1+\bar{p}_2)=-f(\rho_2U_2+\rho_1U_1). \tag{2.6}$$

The first of these is the well-known Margules formula for the slope of a front. We may note here that in meteorological interpretations of this model, $(U_2-U_1)\div(U_2+U_1)$ will normally be much larger than $(\rho_1-\rho_2)\div(\rho_1+\rho_2)$; (2.6) then simplifies to

$$\tan\delta\approx\frac{f\bar{\rho}(U_2-U_1)}{g(\rho_1-\rho_2)}, \tag{2.7}$$

where $\bar{\rho}$ is the mean density,

$$\bar{\rho}=\tfrac{1}{2}(\rho_1+\rho_2). \tag{2.8}$$

This also results directly if ρ_j in (2.2) is replaced by $\bar{\rho}$, an approximation frequently associated with the "Boussinesq" model of incompressible heterogeneous flow.

It is convenient to place the origin of y where the undisturbed frontal surface intersects $z=0$ (Fig. 1). This gives

$$\bar{h}=y\tan\delta. \tag{2.9}$$

The undisturbed front intersects the upper boundary at

$$y=L=H\cot\delta. \tag{2.10}$$

3. Perturbation equations

We allow the steady flow described in Section 2 to be perturbed by a wave-like disturbance, having a small amplitude ϵ, say. The perturbation variables will be of 1st and higher orders in ϵ:

$$\left.\begin{aligned} u_j&=U_j+\epsilon\,\mathrm{Re}\mathfrak{U}_j e^{i\psi}+O(\epsilon^2)\\ v_j&=0+\epsilon\,\mathrm{Re}\mathfrak{V}_j e^{i\psi}+O(\epsilon^2)\\ p_j&=\bar{p}_j+\epsilon\,\mathrm{Re}\mathfrak{P}_j e^{i\psi}+O(\epsilon^2)\\ h&=\bar{h}+\epsilon\,\mathrm{Re}\mathfrak{H}e^{i\psi}+O(\epsilon^2)\\ \psi&=kx+\sigma t \end{aligned}\right\}. \tag{3.1}$$

In the above, U_j are the constant values of Section 2; $\bar{h}$ and $\bar{p}_j$ are the values defined by (2.5) and (2.6); and $\mathfrak{U}_j$, $\mathfrak{V}_j$, $\mathfrak{P}_j$, and $\mathfrak{H}$ are in general complex functions of y; k is the x wavenumber, and σ the frequency.

The 1st order forms of (2.2) are (for $j=1$ and 2),

$$i(\sigma+kU_j)\mathfrak{U}_j-f\mathfrak{V}_j=-\frac{ik}{\rho_j}\mathfrak{P}_j, \tag{3.2}$$

$$i(\sigma+kU_j)\mathfrak{V}_j+f\mathfrak{U}_j=-\frac{1}{\rho_j}\frac{d\mathfrak{P}_j}{dy}, \tag{3.3}$$

while (2.3) and (2.4) yield

$$\mathfrak{P}_1-\mathfrak{P}_2=(\rho_1-\rho_2)g\mathfrak{H}, \tag{3.4}$$

$$i(\sigma+kU_1)\mathfrak{H}=-y\tan\delta\left(ik\mathfrak{U}_1+\frac{d\mathfrak{V}_1}{dy}\right)-\mathfrak{V}_1\tan\delta, \tag{3.5}$$

$$i(\sigma+kU_2)\mathfrak{H}=(H-y\tan\delta)\left(ik\mathfrak{U}_2+\frac{d\mathfrak{V}_2}{dy}\right)-\mathfrak{V}_2\tan\delta. \tag{3.6}$$

Eqs. (3.2) and (3.3) allow $\mathfrak{U}_j$ and $\mathfrak{V}_j$ to be expressed as linear function of $\mathfrak{P}_j$ and $d\mathfrak{P}_j/dy$, i.e.,

$$\mathfrak{V}_j=\frac{i\left[fk\mathfrak{P}_j-(\sigma+kU_j)\frac{d\mathfrak{P}_j}{dy}\right]}{\rho_j[f^2-(\sigma+kU_j)^2]}, \tag{3.7}$$

$$\mathfrak{U}_j=\frac{k(\sigma+kU_j)\mathfrak{P}_j-f\frac{d\mathfrak{P}_j}{dy}}{\rho_j[f^2-(\sigma+kU_j)^2]}. \tag{3.8}$$

Substitution of these expressions in (3.5) and (3.6), followed by elimination of $\mathfrak{H}$ by means of (3.4), results

in two equations for $\mathcal{P}_1$ and $\mathcal{P}_2$:

$$y\frac{d^2\mathcal{P}_1}{dy^2}+\frac{d\mathcal{P}_1}{dy}-\left[k^2y+\frac{kf}{(\sigma+kU_1)}\right]\mathcal{P}_1 = \frac{\rho_1[f^2-(\sigma+kU_1)^2]}{g(\rho_1-\rho_2)\tan\delta}(\mathcal{P}_1-\mathcal{P}_2), \quad (3.9)$$

$$(y-L)\frac{d^2\mathcal{P}_2}{dy^2}+\frac{d\mathcal{P}_2}{dy}-\left[k^2(y-L)+\frac{kf}{(\sigma+kU_2)}\right]\mathcal{P}_2 = \frac{\rho_2[f^2-(\sigma+kU_2)^2]}{g(\rho_1-\rho_2)\tan\delta}(\mathcal{P}_1-\mathcal{P}_2). \quad (3.10)$$

These apply in the frontal region $0\leq y\leq L$. Outside of this range in y, the horizontal velocity must be non-divergent, i.e., $ik\mathcal{U}_j+d\mathcal{V}_j/dy=0$. This leads to two simpler equations for $\mathcal{P}_1$ and $\mathcal{P}_2$:

$$(\sigma+kU_1)\left[\frac{d^2\mathcal{P}_1}{dy^2}-k^2\mathcal{P}_1\right]=0 \quad \text{for} \quad y\geqslant L, \quad (3.11)$$

$$(\sigma+kU_2)\left[\frac{d^2\mathcal{P}_2}{dy^2}-k^2\mathcal{P}_2\right]=0 \quad \text{for} \quad y\leq 0. \quad (3.12)$$

Eqs. (3.9)–(3.12) agree with those used by Kotschin.

Eqs. (3.9) and (3.10) have singularities at $y=0$ and $y=L$, respectively. Finiteness of $\mathcal{U}_j$ and $\mathcal{V}_j$ at $y=0$ and L require that we keep only those solutions of (3.9) and (3.10) which are regular at $y=0$ and L. Thus,

$$\left.\begin{array}{l}\mathcal{P}_1 \text{ regular at } y=0\\ \mathcal{P}_2 \text{ regular at } y=L\end{array}\right\}. \quad (3.13)$$

In addition, we require that $\mathcal{V}_j$, which is given in terms of $\mathcal{P}_j$ by (3.7), be continuous at $y=0$ (for $\mathcal{V}_2$) and $y=L$ (for $\mathcal{V}_1$).

Except for the singular frequencies $\sigma=-kU_j$, finiteness of $\mathcal{P}_1$ at $y=\infty$ and $\mathcal{P}_2$ at $y=-\infty$ requires the solutions of (3.11) and (3.12) to be taken as

$$\mathcal{P}_1(y\geqslant L)\alpha e^{-ky}, \quad (3.14)$$

$$\mathcal{P}_2(y\leq 0)\alpha e^{ky}. \quad (3.15)$$

Continuity of $\mathcal{P}_j$ and $\mathcal{V}_j$ at $y=0$ or L now imposes the following restrictions on the solutions of (3.9) and (3.10):

$$\frac{d\mathcal{P}_1}{dy}=-k\mathcal{P}_1 \quad \text{at} \quad y=L, \quad (3.16)$$

$$\frac{d\mathcal{P}_2}{dy}=k\mathcal{P}_2 \quad \text{at} \quad y=0. \quad (3.17)$$

The mathematical problem is the solution of (3.9)–(3.10) subject to (3.13), (3.16) and (3.17). Before investigating this most general problem, however, it is useful to consider two special limiting cases: (a) *the pure shear waves* which are possible when $\rho_1=\rho_2$ and the front is vertical ($\delta=\pi/2$), and (b), the case of small k.

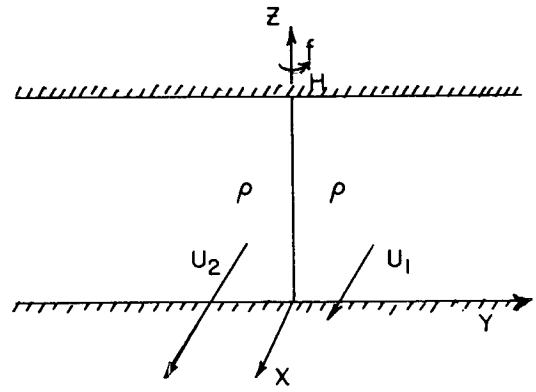

FIG. 2. Shear model.

4. Shear waves

When $\rho_1=\rho_2$, the front is vertical (Fig. 2), and L in (3.11) is zero. The waves now produce a wave-like displacement in y of this vertical interface, i.e.,

$$\Delta(x,t)=\mathrm{Re}De^{i\psi}, \quad (4.1)$$

where D is a constant. The pressure perturbations are as in (3.14) and (3.15):

$$\mathcal{P}_1(y\geqslant 0)=Ae^{-ky}, \quad (4.2)$$

$$\mathcal{P}_2(y\leq 0)=Be^{ky}, \quad (4.3)$$

where A and B are two constants. The dynamic boundary condition is

$$(\mathcal{P}_1-\mathcal{P}_2)_{y=0}=A-B=-f\rho(U_2-U_1)D. \quad (4.4)$$

The kinematic conditions are

$$i(\sigma+kU_1)D=(\mathcal{V}_1)_{y=0}, \quad (4.5)$$

$$i(\sigma+kU_2)D=(\mathcal{V}_2)_{y=0}. \quad (4.6)$$

Using (3.7) with $\mathcal{P}_j$ given by (4.2)–(4.3), we obtain

$$(\mathcal{V}_1)_{y=0}=\frac{ik}{\rho}\frac{[f+\sigma+kU_1]}{[f^2-(\sigma+kU_1)^2]}A, \quad (4.7)$$

$$(\mathcal{V}_2)_{y=0}=\frac{ik}{\rho}\frac{[f-\sigma-kU_2]}{[f^2-(\sigma+kU_2)^2]}B. \quad (4.8)$$

These, together with (4.4)–(4.6), provide three simultaneous homogeneous equations for the three constants D, A and B. Vanishing of the determinant determines σ as a function of U_1, U_2, f and k.

The algebra is simplified by defining

$$\hat{\sigma}=\sigma+k\left(\frac{U_1+U_2}{2}\right), \tag{4.9}$$

$$\bar{U}=\frac{U_2-U_1}{2}, \tag{4.10}$$

and the non-dimensional parameters

$$\mathrm{Ro}=\frac{k\bar{U}}{f}, \tag{4.11}$$

$$\tau=\frac{\hat{\sigma}}{k\bar{U}}=\left[\frac{\sigma}{k}+\tfrac{1}{2}(U_1+U_2)\right]\Big/\tfrac{1}{2}(U_2-U_1). \tag{4.12}$$

Ro is a Rossby number based on the shear of the unperturbed flow, and τ is the negative of the phase velocity relative to the mean flow, divided by half the shear.

Vanishing of the determinant referred to above occurs for four values of τ:

$$\tau=\pm\left(1-\frac{1}{\mathrm{Ro}}\right) \quad \text{and} \quad \tau=\pm i. \tag{4.13}$$

The first pair represent stable inertia waves.[3] The root $\tau=-i$, on the other hand, gives an unstable solution—the well-known phenomenon of shearing instability in homogeneous, incompressible fluids of the same density (Rayleigh, 1879).

Kotschin concluded from his analysis of the general case (3.8)–(3.11) (but for small k) that only stable solutions would exist if the criterion

$$\frac{gH(\rho_1-\rho_2)}{(U_2-U_1)^2\bar{\rho}}=\frac{gH(\rho_1-\rho_2)}{(2\bar{U})^2\bar{\rho}}<2 \tag{4.14}$$

is satisfied. The above analysis of the pure shear waves shows quite clearly, however, that instability can exist even when (4.14) is satisfied.

5. Instability of very long waves

We examine here the behavior of the general problem (3.9)–(3.10) for small k. This will be done, not by putting $k=0$ in (3.9)–(3.10), but by letting k go to zero only after replacing σ by the "phase velocity" τ defined in (4.12), i.e., x-propagation at very small Ro.

It is convenient to define a *Richardson number*,

$$\mathrm{Ri}=\frac{gH}{(U_2-U_1)^2}\left(\frac{\rho_1-\rho_2}{\bar{\rho}}\right)=\frac{fL}{2\bar{U}}, \tag{5.1}$$

and a non-dimensional y coordinate,

$$\eta=\frac{2y}{L}-1. \tag{5.2}$$

The frontal region is located between $\eta=-1$ and $+1$. Kotschin's criterion for stability at k (i.e., Ro$=0$, reproduced in (4.14), corresponds to Ri<2 implying stability in the notation of (5.1).

Eqs. (3.9)–(3.10) may be written as

$$\frac{d}{d\eta}\left[(\eta+1)\frac{d\mathcal{P}_1}{d\eta}\right]-\left[\mathrm{Ri}^2\mathrm{Ro}^2(\eta+1)+\frac{\mathrm{Ri}}{(\tau-1)}\right]\mathcal{P}_1$$
$$=\frac{gH\rho_1(\rho_1-\rho_2)}{2(\rho_2U_2-\rho_1U_1)^2}[1-\mathrm{Ro}^2(\tau-1)^2](\mathcal{P}_1-\mathcal{P}_2)$$
$$\approx\frac{\mathrm{Ri}}{2}[1-\mathrm{Ro}^2(\tau-1)^2](\mathcal{P}_1-\mathcal{P}_2), \tag{5.3}$$

$$\frac{d}{d\eta}\left[(\eta-1)\frac{d\mathcal{P}_2}{d\eta}\right]-\left[\mathrm{Ri}^2\mathrm{Ro}^2(\eta-1)+\frac{\mathrm{Ri}}{(\tau+1)}\right]\mathcal{P}_2$$
$$=\frac{gH\rho_2(\rho_1-\rho_2)}{2(\rho_2U_2-\rho_1U_1)^2}[1-\mathrm{Ro}^2(\tau+1)^2](\mathcal{P}_1-\mathcal{P}_2)$$
$$\approx\frac{\mathrm{Ri}}{2}[1-\mathrm{Ro}^2(\tau+1)^2](\mathcal{P}_1-\mathcal{P}_2). \tag{5.4}$$

The approximation introduced here (also used by Kotschin) is based on the assumed smallness of $(\rho_1-\rho_2)/\bar{\rho}$. It is equivalent to replacing $\bar{\rho}_j$ by $\bar{\rho}$ in the original horizontal equation of motion (2.2). The boundary conditions (3.16)–(3.17) are

$$\left.\begin{aligned}&\frac{d\mathcal{P}_1}{d\eta}=-\mathrm{RiRo}\mathcal{P}_1 \quad \text{at} \quad \eta=1\\&\frac{d\mathcal{P}_2}{d\eta}=\mathrm{RiRo}\mathcal{P}_2 \quad \text{at} \quad \eta=-1\\&\mathcal{P}_1 \text{ and } \mathcal{P}_2 \text{ regular at } \eta=\pm1\end{aligned}\right\}. \tag{5.5}$$

The instability of long waves, the subject of this section, is studied by letting Ro$\to 0$ with k in (5.3)–(5.5). Thus

$$\frac{d}{d\eta}\left[(\eta+1)\frac{d\mathcal{P}_1}{d\eta}\right]-\left[\frac{\mathrm{Ri}}{\tau-1}\right]\mathcal{P}_1=\frac{\mathrm{Ri}}{2}(\mathcal{P}_1-\mathcal{P}_2), \tag{5.6}$$

$$\frac{d}{d\eta}\left[(\eta-1)\frac{d\mathcal{P}_2}{d\eta}\right]-\left[\frac{\mathrm{Ri}}{\tau+1}\right]\mathcal{P}_2=\frac{\mathrm{Ri}}{2}(\mathcal{P}_1-\mathcal{P}_2), \tag{5.7}$$

$$\frac{d\mathcal{P}_1}{d\eta}=0 \quad \text{at} \quad \eta=1; \quad \frac{d\mathcal{P}_2}{d\eta}=0 \quad \text{at} \quad \eta=-1. \tag{5.8}$$

[3] The similar problem analyzed by Haurwitz and Panofsky (1950, p. 726) does not allow the inertia waves because these authors imposed boundaries at finite values of y.

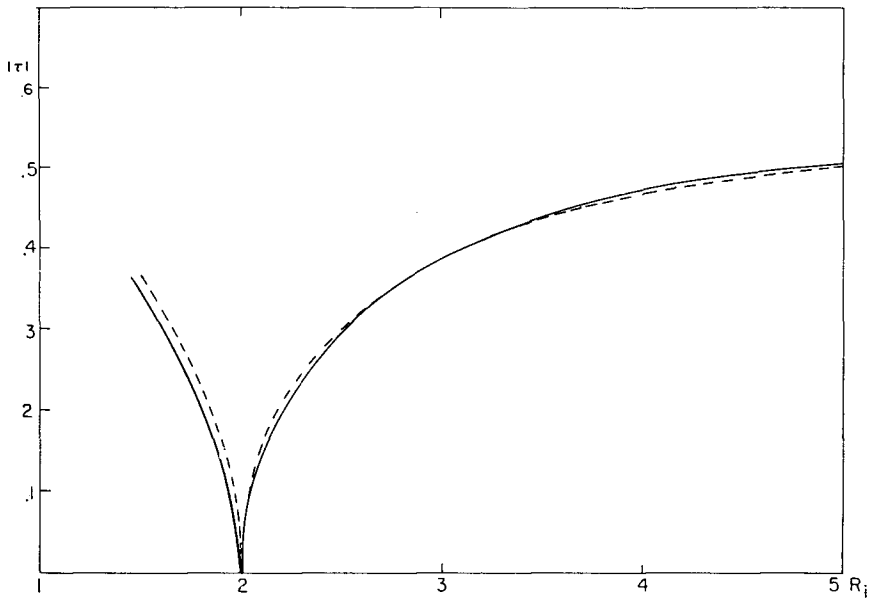

FIG. 3. $|\tau|$ as a function of Ri for Ro=0. The branch for Ri>2 has imaginary τ, the branch for Ri<2 has real τ. The solid curves are the numerical results, the dashed curves are the empirical formula (5.16).

Addition of (5.7) and (5.8) after they have been multiplied by $(\tau-1)$ and $(\tau+1)$ shows that

$$(\tau-1)(\eta+1)\frac{d\mathcal{P}_1}{d\eta}-(\tau+1)(\eta-1)\frac{d\mathcal{P}_2}{d\eta}=\text{constant}=0, \quad (5.9)$$

the zero result being forced by (5.8). It is therefore possible to define

$$\phi(\eta)=(1-\tau)(1+\eta)\frac{d\mathcal{P}_1}{d\eta}=(1+\tau)(1-\eta)\frac{d\mathcal{P}_2}{d\eta}. \quad (5.10)$$

Substituting this in (5.6), differentiating, and substituting (5.10) again, results in the following equations for ϕ:

$$(1-\eta^2)\frac{d^2\phi}{d\eta^2}+(r+s\eta)\phi(\eta)=0; \quad \phi(\pm1)=0, \quad (5.11)$$

where the constants r and s are

$$r=\text{Ri}\left(\frac{1+\tau^2}{1-\tau^2}\right); \quad s=\text{Ri}\left(\frac{-2\tau}{1-\tau^2}\right). \quad (5.12)$$

The case of $\tau=0$ is simple, i.e.,

$$(1-\eta^2)\frac{d^2\phi}{d\eta^2}+\text{Ri}\phi=0; \quad \phi(\pm1)=0. \quad (5.13)$$

The solutions are the integrals of Legendre polynomials, with the boundary conditions being satisfied only if

$$\text{Ri}=\text{Ri}_c=n(n+1), \quad n=1,2,3\cdots. \quad (5.14)$$

If Ri is not equal to 2, 6, 12, etc., $\tau=0$ is not a solution when Ro=0. Kotschin derived his criterion for stability, (4.14), by analyzing the behavior of τ^2 in the vicinity of the first of these neutral solutions (Ri=2).

I have used a numerical variational method (see Appendix) to solve for τ in (5.11) in the range $1.5\leq\text{Ri}\leq5$. Fig. 3 illustrates the results. They agree with Kotschin's conclusion that unstable waves exist for Ri>2. The indication from this figure and (5.14) is that two values of $|\tau_i|$ will be valid for Ri>6, three when Ri>12, etc., but that the $|\tau_i|$ of Fig. 3 will always be greater than the new $|\tau_i|$.

The dashed curve in Fig. 3 is a plot of

$$\tau'=\frac{1}{2\alpha}[\alpha^2-4\alpha\coth\alpha+4]^{\frac{1}{2}}, \quad (5.16)$$

$$\alpha=\frac{4.798}{\text{Ri}}. \quad (5.17)$$

It agrees very closely with the numerical values. The mathematical form of (5.16) is significant in that it agrees with the form of the phase velocity expression derived by Eady (1949) for his *continuously* stratified, baroclinic, *quasi-geostrophic* model. We might expect this since quasi-geostrophic motion is characterized by small Rossby numbers. The qualitative agreement goes even further, however. If one allows a sinusoidal variation with y in Eady's model [see Phillips (1963, pp. 149–150)], with the flow bounded by walls at $y=0$ and

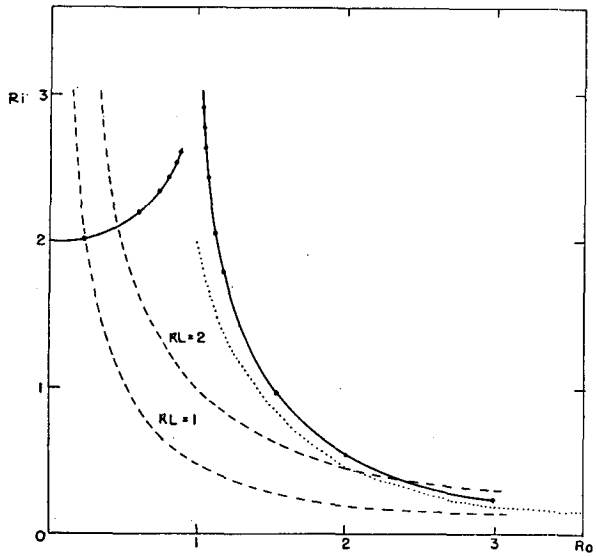

FIG. 4. Location of the roots $\tau=0$ (solid curves) with dots showing individual computed values. The light dotted curve is the asymptote $\mathrm{Ri}=2\ \mathrm{Ro}^{-2}$. The light dashed lines indicate several constant values of the aspect ratio kL.

L_E, the criterion for instability when $k=0$ can be written as

$$\frac{gH}{f^2}\left(\frac{\Delta\rho}{\rho}\right)\frac{m^2\pi^2}{2L_E{}^2}<(2.3994)^2,$$

where m is the number of half wavelengths between $y=0$ and L_E, and $\Delta\rho$ is the density difference from $z=0.75H$ to $z=0.25H$ in Eady's Boussinesq fluid. If we set L_E equal to the L of (2.10) and (5.1), and $\Delta\rho=(\rho_1-\rho_2)$, this may be written as

$$m^2<1.17\ \mathrm{Ri}, \tag{5.18}$$

where Ri is defined by (5.1). Increasing this Ri (keeping L fixed) allows additional wavenumbers in y to become unstable, for $k=0$, in the Eady model. By noting that for large n, Ri_c in (5.14) is equal to n^2, we may not only recognize the physical similarity of the τ_i of Fig. 3 to the now familiar phenomenon of quasi-geostrophic baroclinic instability, but we may conjecture that as Ri increases (with Ro small), additional unstable roots will appear as Ri = 6, 12, etc., and these will have shorter "wavelengths" in the y direction than those unstable roots which have already appeared. Their growth rates will also be less.

It is useful at this point to anticipate some later results. Fig. 10 is an attempt to show the distribution of $|\tau_i|$ as a function of Ri and Ro, for the general system (5.3)–(5.5). The results of the present section, in which Ro = 0, appear on this diagram in the plane Ro = 0 forming the back of the figure in its upper right portion. This plane has an intersection with a curved surface (E) which exists at Ri > 2 and small Ro. This intersection, which is the Ro = 0 boundary of (E), is the curve for Ri > 2 on Fig. 3. The surface (E) on Fig. 10 thus represents the continuation for Ro > 0 of this part of Fig. 3. A second surface, labelled (R), represents additional permissible values of $|\tau_i|$ as a function of Ri and Ro. It overlies (E), and a portion of it has been "cut away" to show the (E) surface. (The detailed shape of these surfaces is determined in Sec. 7). Concerning surface (R), we note first that along the plane Ri = 0, it coincides with the pure shear instability (4.13), $|\tau_i|=1$. Along the plane Ro = 0, i.e., the region discussed in this section, surface (R) also corresponds to $|\tau_i|=1$. However, in distinction to the physically meaningful $|\tau_i|=1$ of surface (R) for Ri = 0, $|\tau_i|=1$ for Ro = 0 has meaning only as a limiting case of small Ro. This is because it corresponds to the trivial solution $\phi=0$ of (5.11), in which $\mathcal{P}_1$ and $\mathcal{P}_2$ are each constant, i.e.,

$$(1+\tau)\mathcal{P}_1=\text{constant}=-(1-\tau)\mathcal{P}_2.$$

Since $k=0$, and $d\mathcal{P}_J/d\eta=0$, $\mathcal{V}_j$ and $\mathcal{U}_j$ vanish identically in this limit, and the "perturbation" is only a redefinition of the basic state.

6. The eigenvalue $\tau=0$

$\tau=0$ corresponds to waves moving with the average speed $\frac{1}{2}(U_1+U_2)$ and undergoing no amplification. We have seen in Section 5 that when Ro = 0 this is possible only for $\mathrm{Ri}=n(n+1)$. As a check of my numerical method, I have computed the values of Ri as a function of Ro which allow τ to vanish in (5.3)–(5.5). These are shown by the heavy dots in Fig. 4. The general shape of the curve formed by smoothly connecting these points agrees with the quantitative description of this curve, with its singularity at Ro = 1, which Kotschin was able to arrive at by analytic means. From Kotschin's analysis, it is also readily shown that the right branch approaches $\mathrm{Ri}=2\ \mathrm{Ro}^{-2}$ for large Ro. This asymptotic curve is indicated by the series of light dots in the figure. It should be pointed out, however, that there are presumably an infinite series of such paired curves, the left-hand member of each pair beginning from the Ri axis (Ro = 0) at Ri = 2, 6, 12, etc. The light dashed curves in Fig. 4 are values of the "aspect ratio"

$$kL=2\ \mathrm{Ri}\ \mathrm{Ro}. \tag{6.1}$$

7. The general case

I have computed solutions of the general problem (5.3)–(5.5) by a numerical method which requires that the regularity conditions for $\mathcal{P}_1$ at $\eta=-1$ and $\mathcal{P}_2$ at $\eta=+1$ be translated into a quantitative rather than a qualitative statement. Consider, for example, (5.3) at $\eta=-1$. $\mathcal{P}_1$ and $d\mathcal{P}_1/d\eta$ must be regular at $\eta=-1$ in order that $\mathcal{U}_1$ and $\mathcal{V}_1$ be finite. At $\eta=-1$, we can there-

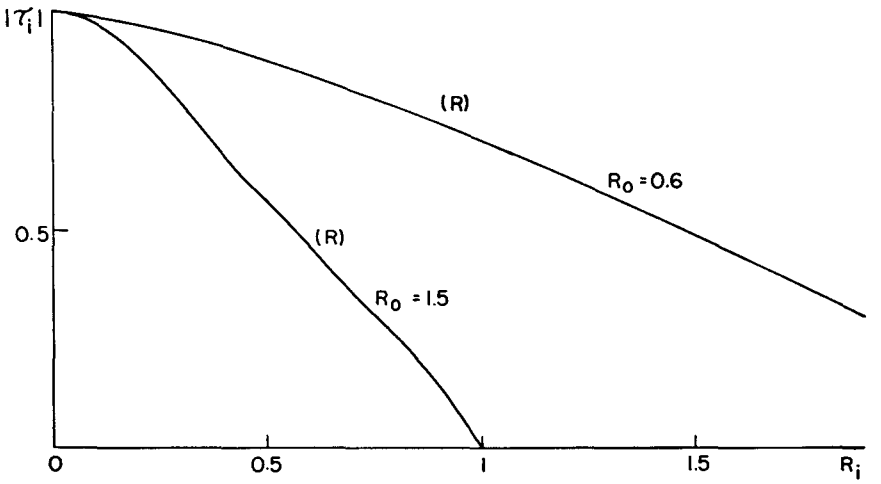

FIG. 5. Continuation into Ri>0, at Ro=0.6 and Ro=1.5, of the pure imaginary τ corresponding to pure shear instability at Ri=0. They are part of the (R) surface of Fig. 12.

fore write

$$(1+\eta)\frac{d^2\mathcal{P}_1}{d\eta^2}+\frac{d\mathcal{P}_1}{d\eta}-\frac{\mathrm{Ri}}{\tau-1}\mathcal{P}_1 = \frac{\mathrm{Ri}}{2}[1-\mathrm{Ro}^2(\tau-1)^2](\mathcal{P}_1-\mathcal{P}_2). \quad (7.1)$$

The first term is not necessarily zero. since $d^2\mathcal{P}_1/d\eta^2$ might be infinite at $\eta=-1$. To show that it should be set equal to zero, we consider the vertical velocity w at the interface h. In this case w is related to $\nabla\cdot\mathbf{v}_j$ by

$$w_1=-z\nabla\cdot\mathbf{v}_1; \quad w_2=(H-z)\nabla\cdot\mathbf{v}_2. \quad (7.2)$$

For the perturbation w in layer 1 in the frontal zone, we find

$$w_1(z=\bar{h})=-y\tan\delta\mathrm{Re}\left[\left(ik\mathcal{U}_1+\frac{d\mathcal{U}_1}{dy}\right)e^{i\psi}\right] = -\mathrm{Im}\left\{\frac{kH(\tau-1)(\eta+1)}{2\bar{\rho}\bar{U}\mathrm{Ri}^2[1-\mathrm{Ro}^2(\tau-1)^2]} \times\left[\frac{d^2\mathcal{P}_1}{d\eta^2}-\mathrm{Ri}^2\mathrm{Ro}^2\mathcal{P}_1\right]e^{i\psi}\right\}. \quad (7.3)$$

At $\eta=-1$ the front intersects $z=0$, and w_1 at $z=\bar{h}$ should approach zero. The above expression shows that this implies $(\eta+1)d^2\mathcal{P}_1/d\eta^2=0$ at $\eta=-1$. Eq. (7.1) is thereby reduced to a quantitative boundary condition relating $\mathcal{P}_1$ and $\mathcal{P}_2$, i.e.,

$$\frac{d\mathcal{P}_1}{d\eta}-\frac{\mathrm{Ri}}{\tau-1}\mathcal{P}_1=\frac{\mathrm{Ri}}{2}[1-\mathrm{Ro}^2(\tau-1)^2](\mathcal{P}_1-\mathcal{P}_2) \quad \text{at} \quad \eta=-1. \quad (7.4)$$

In a similar way, (5.4) will yield a condition at $\eta=+1$. Thus,

$$\frac{d\mathcal{P}_2}{d\eta}-\frac{\mathrm{Ri}}{\tau+1}\mathcal{P}_2=\frac{\mathrm{Ri}}{2}[1-\mathrm{Ro}^2(\tau+1)^2](\mathcal{P}_1-\mathcal{P}_2) \quad \text{at} \quad \eta=+1. \quad (7.5)$$

We now have the two second-order equations (5.3)–(5.4), with the four homogeneous boundary conditions (5.5) and (7.4)–(7.5), for the variables $\mathcal{P}_1$ and $\mathcal{P}_2$. Being interested in complex τ, we expect that $\mathcal{P}_1$ and $\mathcal{P}_2$ will be complex.

I have explored the solutions of this system by a numerical method (Appendix A), for the general range $0\leq\mathrm{Ri}\leq5$, $0\leq\mathrm{Ro}\leq3$, and with primary emphasis on non-real values of τ. Fig. 19 in Appendix A shows the location of the Ri-Ro points studied. Appendix C lists all the τ-values for these points. Fig. 10 summarizes graphically the location of the $|\tau_i|$ surfaces which I have found in this region of Ri-Ro space. This figure will be more intelligible, however, if the values of τ along certain cuts in Ri-Ro space are first described. This is done in Figs. 5–12.

In one part of this Ro-Ri region—small Ro and Ri>2—the computations give two distinct values of $|\tau_i|$ for each Ro-Ri point, where τ_i is the imaginary part of τ. In the remainder of this Ro-Ri region, only one value of $|\tau_i|$ for each Ro-Ri point is discovered by the numerical work. (It should be noted that if $\tau=\tau_1$ is a solution, $-\tau_1$, τ_1^*, and $-\tau_1^*$ are also solutions. The change $\tau\rightarrow-\tau$ corresponds to interchanging $\mathcal{P}_1$ and $\mathcal{P}_2$ and changing the sign of η, an intuitively obvious symmetry.)

Fig. 5 shows, at constant Ro, the continuation into Ri>0 of the pure shear wave instability described in Section 4. This τ root remains imaginary for some range in Ri. When Ro>1, it vanishes along the right-hand curve, $\tau=0$, of Fig. 4. At this point, although not shown on Fig. 5, a complex value of τ appears. An example of

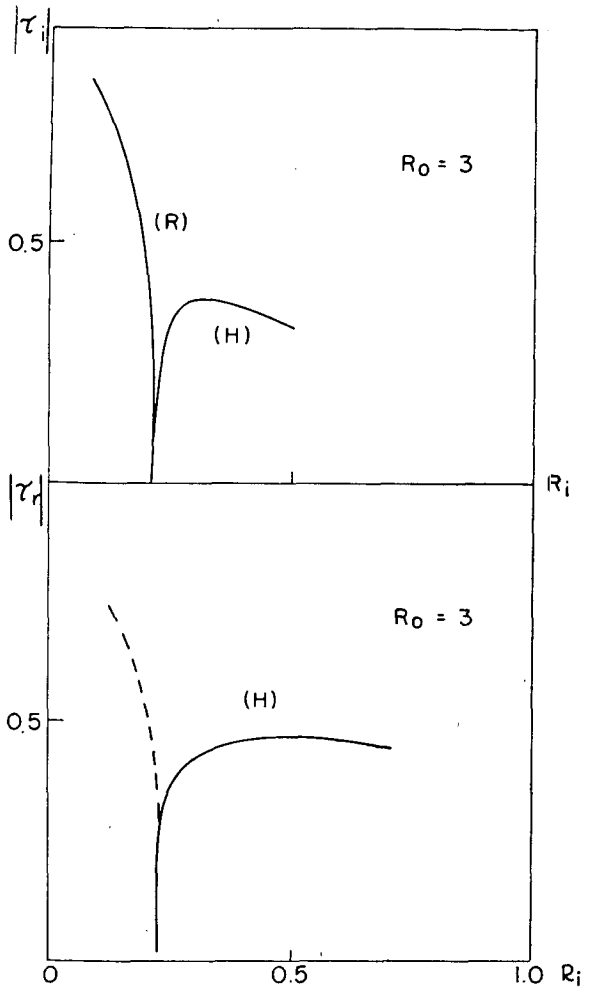

FIG. 6. (Upper diagram) transition from the pure imaginary τ root of (R) to the complex τ root of surface (H) as Ri increases when Ro=3. The lower diagram shows a separate real root coexisting with the imaginary τ of (R), and the real part of the complex τ of (H).

this behavior is shown on the upper part of Fig. 6. (The lower part of Fig. 6 shows a coexisting real root at small Ri.) In anticipation of Fig. 10, it will be convenient to refer generally to the $|\tau_i|$ surface of which a portion is shown in Fig. 5 and the small Ri portion of the upper part of Fig. 6 as the (R) surface, and to refer to the complex $|\tau_i|$ appearing on the right side of Fig. 6 as the (H) surface.

Figs. 7–8 show the τ behavior with Ro at successively larger constant values of Ri. Fig. 7 contains curves of $|\tau_i|$ at three values of Ri (1.9, 2.03, 2.1) near the critical value Ri=2 discussed in Section 5. At Ri=2.03, we see a new phenomenon, the appearance of a second $|\tau_i|$ at small Ro. This is the extension into Ro>0 of the unstable curve shown on Fig. 3. This root is pure imaginary, as it was on Fig. 3. We shall refer to this $|\tau_i|$ surface as surface (E).

A further increase in Ri to 2.1 shows (on Fig. 7) that (E) and (R) now coalesce into a new surface. This surface will be referred to as (B) where τ is complex. Therefore, the progression from Ro=0 to Ro=0.5 at Ri=2.1 does not involve a change in the number of roots for which $|\tau_i| \neq 0$; to the left of the intersection of (R) and (E) there are four pure imaginary roots, while surface (B) represents four complex roots having equal $|\tau_i|$. Surface (B) goes to zero on the left-hand curve of Fig. 4. At larger Ro (still at Ri=2.1) the surface is again like that of (R), with two pure imaginary roots.

Fig. 8 reproduces in its upper part the Ri=2.1 curve of Fig. 7. It extends to larger Ro and shows the (H) surface which appears at Ro>1.1. The collection of roots in this figure correspond to four consistent solutions. At $0.4 \leq Ro \leq 0.5$ and Ro>1.1, the four roots are complex (consisting of τ, $-\tau$, τ^* and $-\tau^*$). They are dashed and are part of surfaces (B) and (H). Between these are located two imaginary roots (τ and $-\tau=\tau^*$) of surface (R) shown as solid curves and two real roots (dotted). At Ro<0.4, the four roots consist of two pure imaginary roots on each of surfaces (R) and (E). The roots pass through zero at the intersection of the $\tau=0$ curves of Fig. 4.

At $Ri \geq 2.2$ a more complicated behavior appears at Ro>1. The (R) surface, which until now has represented two pure imaginary roots of equal magnitude, seems to represent complex τ's at Ro>1.05. Repeated attempts to find numerically additional τ's at this Ri were made, but did not succeed. On Fig. 8, the inter-

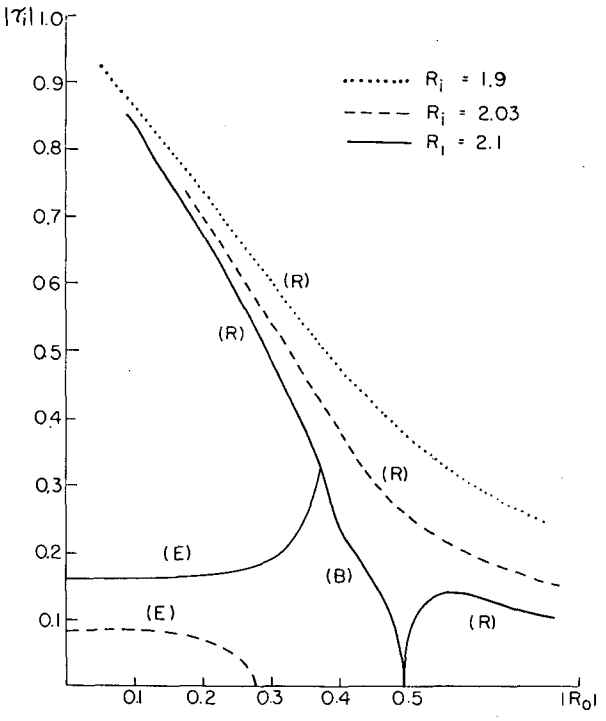

FIG. 7. Values of $|\tau_i|$ as a function of Ro for 3 values of Ri in the vicinity of the critical value Ri=2. All τ_i are pure imaginary except the curve (B).

section with the $\tau=0$ curves of Fig. 4 (at Ro$\sim$0.5 and 1.1) are clear. At large Ri, however, no indication of the second of these intersections was found. The numerical method I used is sensitive in the neighborhood of $\tau=0$ (Appendix A), and this may be the reason for this behavior. Another possibility is that the seemingly clear-cut roots at smaller Ri are really multiple roots.

Fig. 9, at Ri=5, contains all the non-real τ values that I was able to discover by the numerical method. Pure imaginary τ's were found only at very small Ro, where the (E) and (R) surfaces may be seen on the left side of the upper half of this figure. The complex τ of (B) is still present.

We are now prepared to examine Fig. 10, which is a three-dimensional plot of surfaces of $|\tau_i|$ as a function of Ro and Ri. Four separate surfaces are shown, labelled (R), (H), (E) and (B). These surfaces occupy mutually exclusive regions of this Ri-Ro space, except where Ro is small and Ri>2. In this region (E) lies underneath (R), and a portion of the latter has therefore been "cut away" to allow (E) to be seen.

The shape of (R) and (H) is indicated by the shaded profiles at constant values of Ri (0, 0.5, 1.0, 1.5 and 1.9), and by the isolines of $|\tau_i|$. (R) and (H) are separated by an isoline $|\tau_i|=0$ (the right branch of $\tau=0$ in Fig. 4), but this isoline is hidden in the figure by the intervening (H) surface. The separation between (R) and (H) is unclear at Ri>2 and Ro$\gtrsim$1, where the numerical method converged poorly. The value of $|\tau_i|$ on (H) decreases with increasing Ri and Ro for large Ri and Ro. The imaginary part of σ, the *growth rate*, is proportional to (Roτ_i). At constant Ro (constant k), an increase of Ri can be achieved by increasing

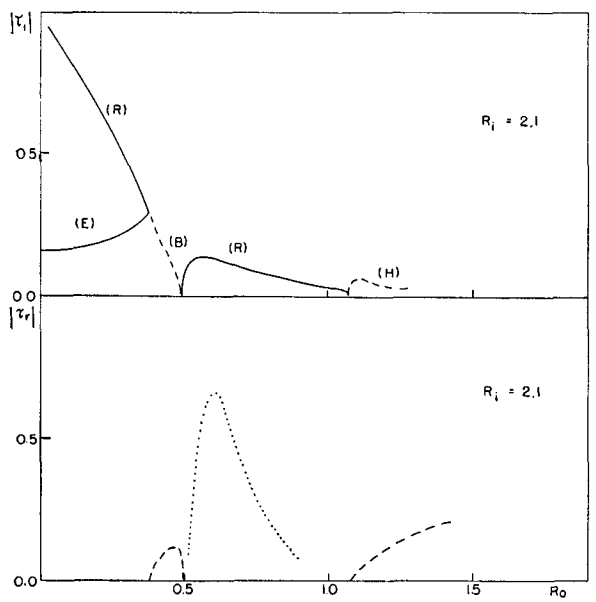

FIG. 8. Absolute values of the imaginary and real parts of a consistent set of four roots τ, as a function of Ro at Ri=2.1. Imaginary roots are solid, complex roots are dashed, and real roots are dotted.

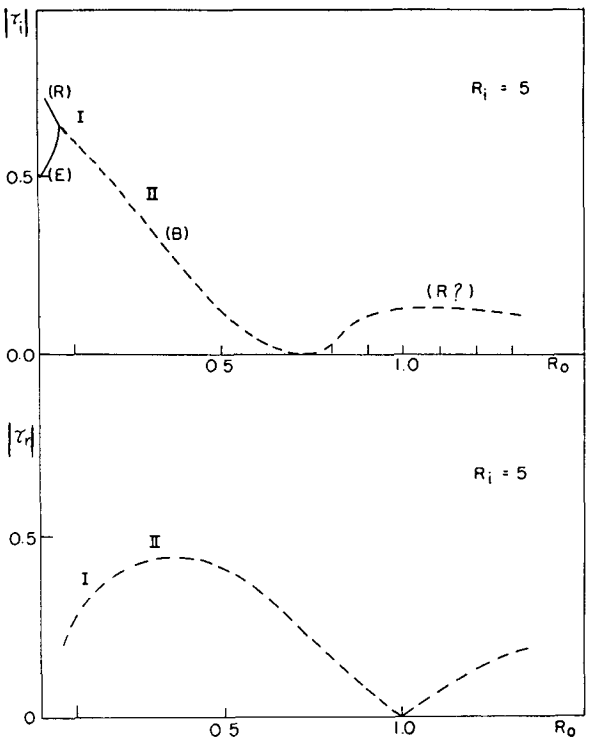

FIG. 9. Absolute values of the imaginary and real parts of τ as a function of Ro at Ri=5. Imaginary roots are solid, complex roots are dashed. Points I and II identify the Ro and Ri points for which kinematic and energy computations are described in Sections 8 and 9.

$(\rho_1-\rho_2)/\bar{\rho}$. From a physical point of view, this increase in static stability is therefore consistent with the generally decreasing value of the numerically computed $|\tau_i|$ of surface (H) as Ro (i.e., k) is kept constant and Ri is increased. At Ri=constant <2, the growth rate has one maximum associated with (R) and one with (H). The latter is larger.

Surface (H) is labelled as such because it seems to correspond to Helmholtz instability, modified, of course, by the Coriolis force and frontal geometry. [See also comment a. later.] In the absence of rotation (so that the front becomes horizontal) hydrostatic Helmholtz instability has the τ formula,[4]

$$\tau^2=\mathrm{Ri}-1, \tag{7.6}$$

for waves in which $\partial/\partial y$ and v are zero. This expression, which one would expect to be valid at large Ro, gives stability at Ri>1; and $|\tau_i| \to 1$ for Ri$\to$0. The latter limit seems to be a reasonable one for the max $|\tau_i|$ on the (H) surface of Fig. 10 as Ro$\to\infty$, where the (H) surface extends to Ri=0 (Fig. 4). Eq. (7.6) also suggests the possibility of a curve Ri=Ri$_H$(Ro) extending in from Ro$=+\infty$, along which the $|\tau_i|$ of (H) vanishes, but the corresponding $|\tau_r|$ does not. This would not correspond to one of the Kotschin $\tau=0$ curves, and, if

[4] The small density ratio approximation introduced in (5.3) and (5.4) is also used here.

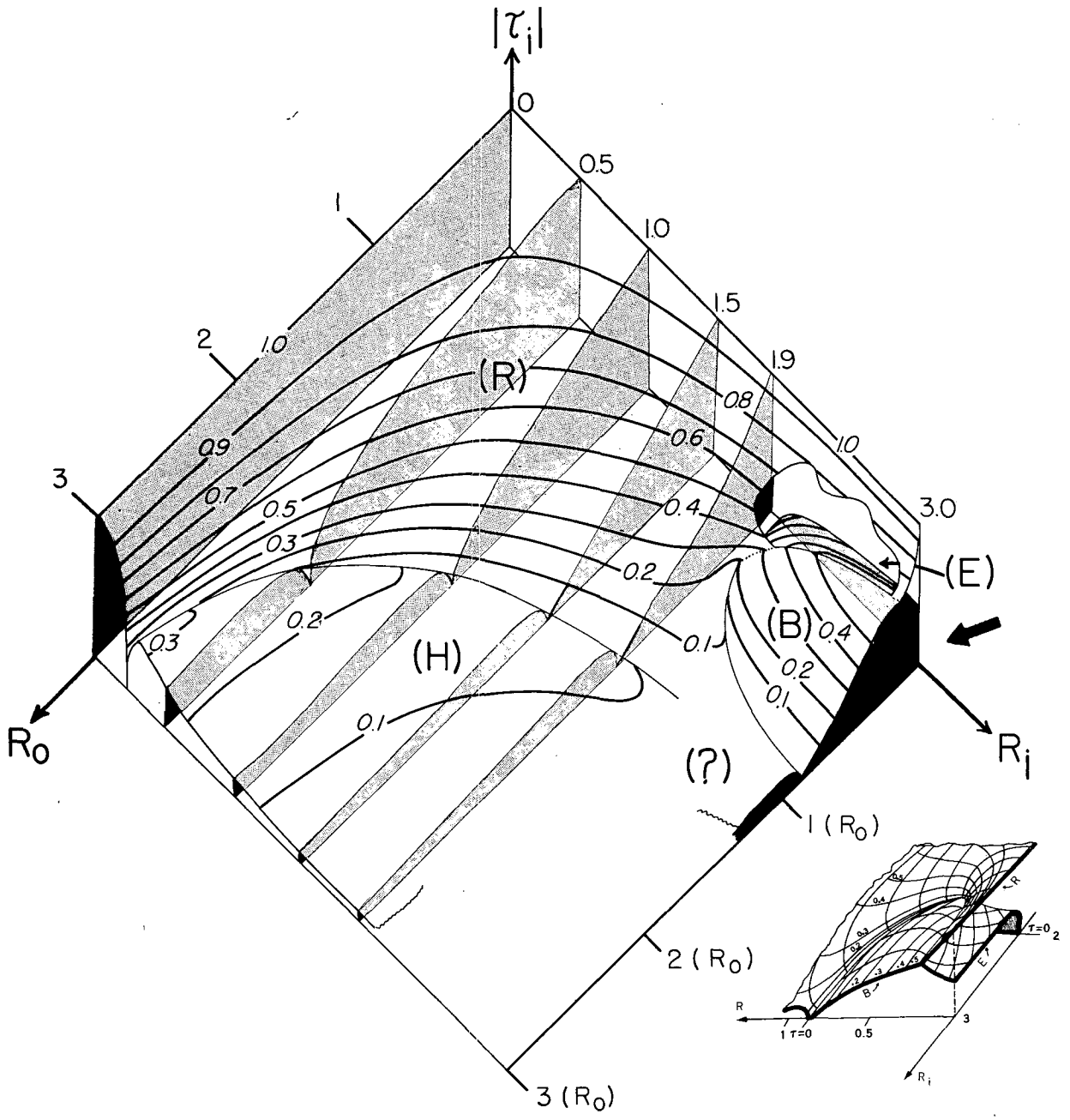

FIG. 10. The *main figure* is a three-dimensional diagram showing $|\tau_i|$ = growth rate $\div kU$ as a function of $\mathrm{Ri}=gH\Delta\bar{\rho}/\rho 4U^2$ and $\mathrm{Ro}=kU/f$. Isolines of $|\tau_i|$ are shown by labelled (heavy) solid curves on the four surfaces (H), (R), (E), (B). Profiles of (H) and (R) are shown by the shaded sections at several constant values of Ri (0. 0.5, 1.0, 1.5, and 1.9). A portion of (R) has been cut away to show the underlying (E) surface. Light solid (and dotted) lines are not isolines of $|\tau_i|$, but indicate boundaries of the surfaces and profiles. In three cases—between (R) and (H), to the lower left of the symbol (B), and at the left-most extension of (E)—these light solid lines represent the silhouette boundaries introduced by the perspective view rather than the actual limits of the surfaces. The *small figure* illustrates a different view (arrow) of the right corner of the main figure. Lines of constant $|\tau_i|$ and their orthogonal curves are shown.

present, might explain, at Ro$\sim$1, the difficulties encountered on Fig. 9.

The (R) surface in Fig. 10 extends to both coordinate axes where it takes on the value $|\tau_i|=1$. On the Ro axis (Ri=0), it corresponds to Rayleigh shear instability as described in Section 4, while on the Ri axis (Ro=0) it corresponds to the trivial solution $\phi=0$ described at the end of Section 5.

The third instability surface (E) is visible in the right corner of Fig. 10, where a portion of the (R) surface, which *overlies* (E), has been cut away. (E) begins, at Ro=0, from the right branch (Ri>2) of the

curve in Fig. 3. (This part of the Ro=0 plane is lightly shaded in Fig. 10). From this position it generally slopes up with increasing Ro, eventually intersecting the oppositely sloping (R). This intersection of (R) and (E) is shown by dotted lines in the uncut portion and by a light solid line where (R) has been cut away. This intersection curve has positive $d\,\mathrm{Ri}/d|\tau_i|$ and negative $d\,\mathrm{Ro}/d|\tau_i|$, at least for $\mathrm{Ri}\leq 5$ (Fig. 9).(E) is bounded at $|\tau_i|=0$ by a portion of the left branch of the $\tau=0$ curve in Fig. 4.

The fourth surface (B) extends from the intersection of (R) and (E) down to the remaining part of the left $\tau=0$ curve in Fig. 4. In distinction to the (H), (R) and (E) surfaces, which represent pure imaginary τ, (B) represents complex τ values.

The $|\tau_i|=0$ boundary of (B) and (E), like its companion curve separating (H) and (R), is not visible in Fig. 10, being hidden by intervening surfaces. It is located close to the light continuous solid line marking the silhouette boundaries of (R) and (E). The critical point on it which marks its intersection with the curve separating (B) and (E) is located near Ri=2.05, Ro=0.35. This point is also hidden in Fig. 10, but would be located close to the point where the $|\tau_i|=0.2$ isolines of surfaces (R) and (B) give the appearance of meeting. (All three surfaces are steep near this point.)

The growth rate σ_i is equal to

$$\sigma_i = f\,\mathrm{Ro}\tau_i.$$

A graph of this is shown for Ri=3 in Fig. 11. There are two maxima. At Ro<1, the maximum is on surface (B). At larger values of Ri, this maximum remains on (B), decreasing slowly in magnitude. (R) and (E) are confined to even smaller values of Ro and growth rates at larger Ri. The nature of the second maximum at Ro=1.1 on Fig. 11 is not completely clear. The numerical computations indicate that it moves to larger Ro as Ri increases. It appears to be a continuation of the (R) surface from smaller Ri.

The numerical method computes the eigenfunctions $\mathcal{P}_j$ as the value of τ is determined, and the kinematic character of the different wave motions can then be determined by using (3.7), (3.8) and (7.3). (This is not unique, however, since Ri and Ro are insufficient to specify $\mathcal{U}_j$, $\mathcal{V}_j$ and $\mathcal{W}_j$ as a function of $\mathcal{P}_j$; k or $\bar{U}/f$ is also required.) My computations indicate the following typical features of the kinematics.

a. For Ri<2, we have only the (R) and (H) instabilities. The particle motion in the wave for (R) is generally quasi-horizontal, even in the frontal zone. As Ro is increased at constant Ri<2, by increasing k, this motion tends to become less horizontal. As the curve $\tau=0$ separating (R) and (H) is passed, the motion becomes more vertical. Whereas (R) waves in the limit of zero Ro or zero Ri are characterized by zero vertical velocity and a balance between $\partial u/\partial x$ and $\partial v/\partial y$, the waves for (H) become characterized, at large Ro, by zero meridional velocity and a balance between $\partial u/\partial x$ and $\partial w/\partial z$. We may therefore characterize surface (R) as representing quasi-horizontal wave motion which is unstable due to *horizontal* shear. Surface (H) represents Helmholtz instability (see Lamb, p. 374) with a stabilizing effect of gravity and a destabilizing effect of *vertical* shear.[5]

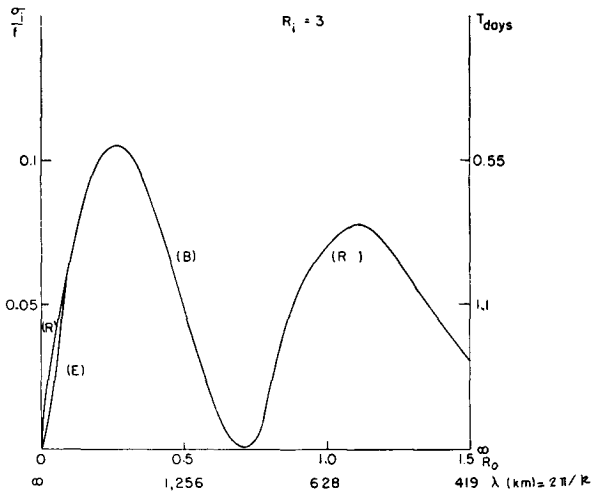

FIG. 11. Growth rate $\sigma_i/f=\mathrm{Ro}\tau_i$ as a function of Ro for Ri=3. The corresponding doubling time in "days" (1 day$=4\pi f^{-1}$) is shown on the right scale. A wavelength scale is shown on the abscissa for $U=10$ m sec^{-1}, $f=10^{-4}$ sec^{-1}.

b. When Ri>2, there is a region at small Ro where two distinct instability surfaces, (R) and (E), exist. The wave for (R) has particle motion which is more horizontal than that in the wave for (E) (at the same Ri, Ro and k). The former still has a near balance between $\partial u/\partial x$ and $\partial v/\partial y$. At Ri only slightly greater than 2, none of the three contributions to $\partial u/\partial x+\partial v/\partial y+\partial w/\partial z$ are negligible for surface (E). At Ri=5, however, there is also quasi-horizontal motion for surface (E), as shown in the next section. The interface is deformed only slightly for (R) waves compared to the deformation present in the (E) waves. This is related to the different energy sources for these waves. It is shown in Section 9 that the transformation of mean potential energy to wave energy is proportional to the interface deformation. The smallness of the latter in (R) waves means that these can only obtain energy from the mean kinetic energy, and may be referred to then as *barotropic* instabilities. Surface (E) waves on the other hand, receive energy from the mean potential energy and are *baroclinic* instabilities.

A detailed example of the kinematics for surface (B) is presented in the following section for large Ri (=5) and small Ro (0.1). The wave motion at this point on (B) is quasi-horizontal, in that $\partial u/\partial x$ and $\partial v/\partial y$ tend to cancel. This is not necessarily true for all points on

[5] At large k, the hydrostatic assumption used in (2.2)–(2.4) is of course a poor one. For example, Helmholtz instability (Lamb, 1936, p. 374) exists for all Ri at sufficiently large k in the non-hydrostatic case, but does not exist for any k if Ri>1 where the hydrostatic assumption is used.

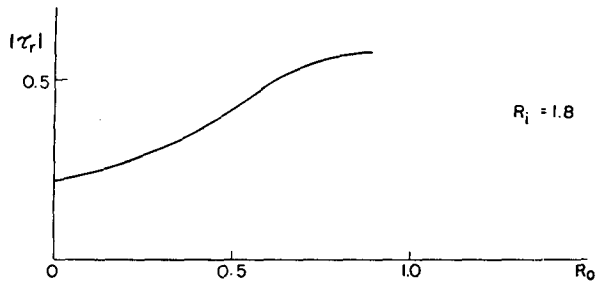

FIG. 12. Continuation into Ro>0 at Ri=1.8 of the real τ root of Fig. 3.

surface (B), however; larger Ro and smaller Ri reduce the quasi-horizontal nature of the motion.

Because of the difficulties experienced in the numerical method for Ri>2 and Ro>1, the kinematics in this region are not very clear.

The emphasis has been placed here on imaginary and complex values, but the numerical method can compute real τ's as well. An example is shown in Fig. 12, for Ri=1.8. This root is the continuation for Ro>0 of the neutral branch (the left-hand curve) in Fig. 3. This real τ surface also appears on the lower left side of Fig. 6, where it presumably joins up at Ri=0 with the neutral inertia waves of (4.13) in the shear model.

A final remark pertinent here concerns the instability described by Fultz (1952) in an experimental two-fluid system. Using (2.7) and (5.1) we may write

$$\mathrm{Ri}=\frac{f^2\bar{\rho}H}{g(\rho_1-\rho_2)\tan^2\delta}.$$

The instabilities found by Fultz seem to have occurred with $\tan\delta\sim 1$, $f\sim 0.4$ sec^{-1}, $H\sim 5$ cm, $g\Delta\rho/\rho\sim 5$. This gives Ri=0.16, suggesting that these instabilities may be closer to a barotropic shear instability than to a true baroclinic instability.

8. Kinematics of a meteorological frontal wave

In this section I describe the velocity, pressure and divergence fields associated with an unstable frontal wave. The parameters are:

$$\begin{gathered}U_2=15\text{ m sec}^{-1}\\ U_1=-5\text{ m sec}^{1}\\ f=10^{-4}\text{ sec}^{-1}\\ (\rho_1-\rho_2)=2\times10^{-5}\text{ ton m}^{-3}\\ \bar{\rho}=10^{-3}\text{ ton m}^{-3}\\ H=10^{4}\text{ m}\\ k=2\pi/\lambda=10^{-6}\text{ m}^{-1}\\ g=10\text{ m sec}^{-2}\end{gathered}$$

These give the following derived parameters:

$$\bar{U}=(U_2-U_1)/2=10\text{ m sec}^{-1}$$

$$\mathrm{Ro}=k\bar{U}f^{-1}=10^{-1}$$

$$\mathrm{Ri}=\frac{gH(\rho_1-\rho_2)}{4\bar{\rho}\bar{U}^2}=5$$

$$\frac{d\bar{h}}{dy}=\tan\delta=\frac{2f\bar{\rho}\bar{U}}{g(\rho_1-\rho_2)}=10^{-2}$$

$$L=H\cot\delta=10^{6}\text{ m}$$

$$\lambda=2\pi k^{-1}=6.28\times10^{6}\text{ m}$$

The values of Ro and Ri place this point in surface (B), with a numerically computed τ value of

$$\tau=0.30281-0.5957i. \qquad (8.1)$$

(This is the point labelled I on Fig. 9). The growth

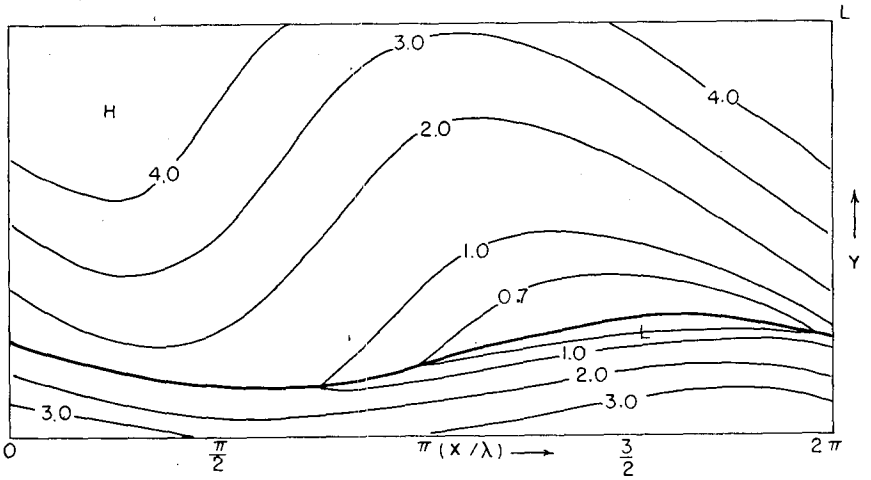

FIG. 13. Total pressure field at $z=1750$ m (perturbation plus basic state) in the frontal zone, $0<y<1000$ km. Layer 2 (the "upper" layer) is in the bottom of the figure, layer 1 (the "lower" layer) is in the top of the figure. The deformed frontal surface is the heavy curve. Units are in millibars.

rate, $k\bar{U}|\tau_i|$ is equal to 0.5957×10^{-5} sec^{-1}, corresponding to a doubling time of 32.5 hr. The real part of the phase speed is 1.97 m sec^{-1} in the positive x direction, approximately 3 m sec^{-1} slower than the mean flow of 5 m sec^{-1}.

The above numbers were chosen to coincide roughly in magnitude with the parameters which have been thought of as characterizing the "cyclone" unstable wave, by earlier writers.[6] Ri is the same as that used by Eliasen in his example (with a wall at $y=L/2$), but he used a slightly larger Ro of 0.3. The amplitude of the perturbation is arbitrary, but the units given in the figures are consistent.

Fig. 13 shows the total pressure field (perturbation plus basic flow) at $z=1750$ m in the frontal zone, $0\leq y\leq L$. The intersection of the deformed frontal surface with this constant height surface is shown by the heavy line. Fig. 14 shows the real and imaginary parts of $\mathfrak{U}_1$ and $\mathfrak{V}_1$, in the frontal zone, by solid curves. The dashed curves are the "geostrophic" values, defined by neglecting all terms in (3.7) and (3.8) not containing the Coriolis parameter f, i.e.,

$$\mathfrak{V}_j=\frac{ik\mathcal{P}_j}{f\bar{\rho}},$$

$$\mathfrak{U}_j=-\frac{1}{f\bar{\rho}}\frac{d\mathcal{P}_j}{dy}.$$

The agreement with the actual $\mathfrak{U}_j$ and $\mathfrak{V}_j$ is very close, undoubtedly a reflection of the large Ri and small Ro characterizing this example.

Fig. 15 presents the fields of $-(H/2)\nabla\cdot\mathbf{v}_1$ and $+(H/2)\nabla\cdot\mathbf{v}_2$. These quantities have the same sign as the vertical velocity w in each layer, and correspond in magnitude to the vertical velocity that would exist at $z=H/2$ in each layer, if the layer extended above (or below) $z=H/2$. The location of the pressure trough ($-$) and ridge ($+$) are shown also. From these we see that in the lower layer horizontal divergence is positively correlated with perturbation pressure and the opposite in the upper layer. Fig. 16 shows that the perturbation amplitude is largest in layer 2, especially at $y\sim L$.

A significant feature of the perturbation velocity field is the relative magnitude of $\partial u/\partial x$, $\partial v/\partial y$, and their sum, $\nabla\cdot\mathbf{v}=\partial u/\partial x+\partial v/\partial y$. The maximum value of $\nabla\cdot\mathbf{v}_1$ from Fig. 15 is somewhat less than 2×10^{-7} sec^{-1}. The magnitudes of $\partial u/\partial x$ and $\partial v/\partial y$ can be estimated from Fig. 14 as 9×10^{-7} and 6×10^{-7} sec^{-1}, respectively, showing that there is partial compensation between $\partial u_1/\partial x$ and $\partial v_1/\partial y$. The same quasi-balance occurs in layer 2, where the two-fold increase in $\nabla\cdot\mathbf{v}$ apparent on

[6] At this value of Ri (5.0), the maximum growth rate occurs at Ro=0.3, the point labelled II on Fig. 9. This would have a wavelength λ of 2090 km, but the general kinematics would be similar to the present example, although less geostrophic.

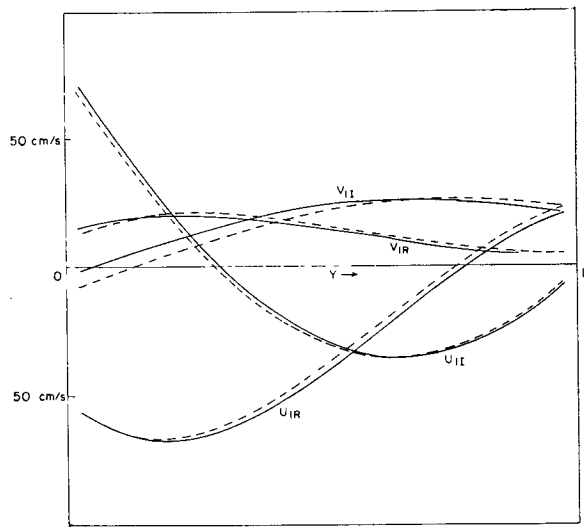

FIG. 14. Graphs of the real and imaginary parts of the velocity amplitudes $\mathfrak{U}_1(y)$ and $\mathfrak{V}_1(y)$ in the frontal zone (solid curves), in cm sec^{-1}. The dashed curves are the geostrophically evaluated functions.

Fig. 15 is accompanied by a corresponding increase in $\mathcal{P}$ and $\mathbf{v}$ (Fig. 16).

A second unstable solution, with τ equal to the negative conjugate of (8.1) also exists, since (B) represents complex τ. Thus,

$$\tau=-0.30281-0.5957i. \tag{8.2}$$

The corresponding eigenfunctions are the conjugates of those belonging to (8.1), with the subscripts 1 and 2 interchanged, and η replaced by $-\eta$. This wave has a phase speed greater than the mean flow of 5 m sec^{-1}, and has a maximum amplitude in layer 1.

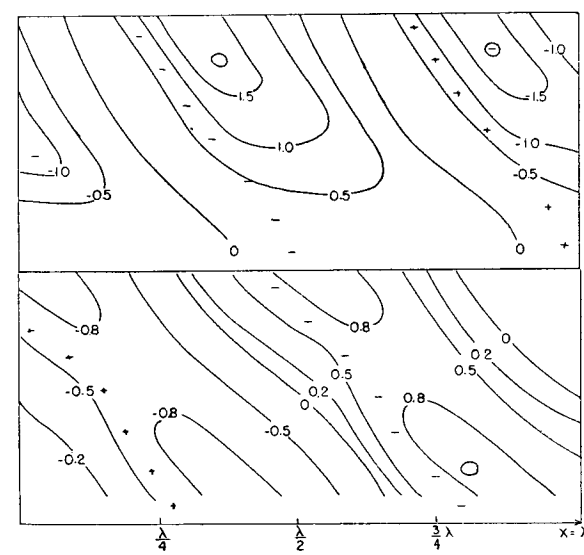

FIG. 15. Fields of $+\frac{1}{2}H\nabla\cdot\mathbf{v}_2$ (upper) and $-\frac{1}{2}H\nabla\cdot\mathbf{v}_1$ (lower) in the frontal zone. The series of $+$'s and $-$'s show the location of the pressure ridge and trough in each layer. Units are 10^{-3} m sec^{-1}.

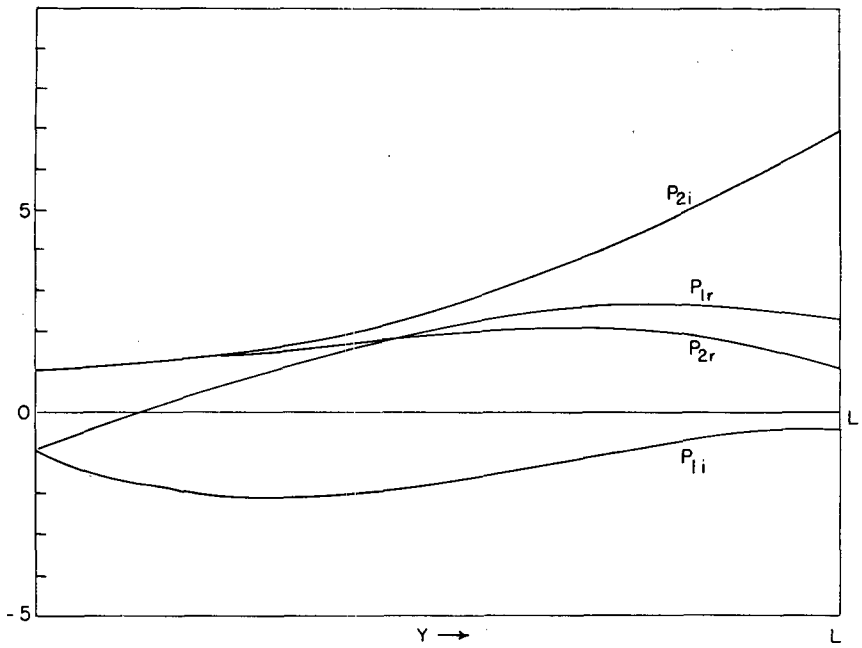

FIG. 16. Pressure amplitudes $\mathcal{P}_1$ and $\mathcal{P}_2$ in the frontal zone. Units are millibars.

9. Energy transformations

The energy equation for this model can be derived from the fundamental equations (2.2)–(2.4) as follows. Multiplication of (2.2) with $\rho_1 h\mathbf{v}_1$ for $j=1$ and $\rho_2(H-h)\mathbf{v}_2$ for $j=2$, followed by addition of (2.4) multiplied by $\frac{1}{2}\rho_1\mathbf{v}_1^2$ and $\frac{1}{2}\rho_2\mathbf{v}_2^2$, gives

$$\frac{1}{2}\frac{\partial}{\partial t}[\rho_1 h\mathbf{v}_1^2+\rho_2(H-h)\mathbf{v}_2^2]$$

$$=-\nabla\cdot[h\mathbf{v}_1(p_1+\tfrac{1}{2}\rho_1\mathbf{v}_1^2)+(H-h)\mathbf{v}_2(p_2+\tfrac{1}{2}\rho_2\mathbf{v}_2^2)]$$

$$+[(\rho_1-\rho_2)gh+\rho_2 gH][\nabla\cdot h\mathbf{v}_1]. \quad (9.1)$$

The boundary conditions are cyclic continuity in x and that v vanish at $|y|=\infty$. An area integral over a wavelength in x and $-\infty\leq y\leq\infty$ will be denoted simply by

$$\int(\ )da.$$

Thus,

$$\frac{1}{2}\frac{\partial}{\partial t}\int[\rho_1 h\mathbf{v}_1^2+\rho_2(H-h)\mathbf{v}_2^2]da$$

$$=(\rho_1-\rho_2)g\int h\nabla\cdot h\mathbf{v}_1 da. \quad (9.2)$$

Multiplying (2.4) by $(\rho_1-\rho_2)gh$ and integrating, we find

$$\frac{1}{2}\frac{\partial}{\partial t}\int(\rho_1-\rho_2)gh^2da=-(\rho_1-\rho_2)g\int h\nabla\cdot h\mathbf{v}_1 da. \quad (9.3)$$

The interpretation is obvious: left sides represent the time rates of change of kinetic and potential energy in the system, while the right sides represent a transformation between kinetic and potential energy.

Let us now introduce the concept of an x average, denoted by angular parentheses, and a deviation from that average, denoted by a prime:

$$\left.\begin{aligned}\langle f\rangle&=\frac{1}{\lambda}\int_0^\lambda f dx,\\ f'&=f-\langle f\rangle;\quad\langle f'\rangle=0\end{aligned}\right\}. \quad (9.4)$$

We define

K_M = kinetic energy of mean motion

$$=\frac{1}{2}\int[\rho_1\langle h\rangle\langle\mathbf{v}_1\rangle^2+\rho_2(H-\langle h\rangle)\langle\mathbf{v}_2\rangle^2]da, \quad (9.5)$$

P_M = potential energy of mean motion

$$=\frac{1}{2}\int(\rho_1-\rho_2)g\langle h\rangle^2 da, \quad (9.6)$$

K_I = interaction kinetic energy of deviation from mean flow

$$=\int[\rho_1\langle\mathbf{v}_1\rangle\cdot\langle h'\mathbf{v}_1'\rangle-\rho_2\langle\mathbf{v}_2\rangle\cdot\langle h'\mathbf{v}_2'\rangle]da, \quad (9.7)$$

K_E = quadratic kinetic energy of deviation from mean flow

$$=\frac{1}{2}\int[\rho_1\langle h\rangle\langle\mathbf{v}_1'^2\rangle+\rho_2(H-\langle h\rangle)\langle\mathbf{v}_2'^2\rangle]da, \quad (9.8)$$

P_E = potential energy of deviation from mean flow

$$= \tfrac{1}{2}(\rho_1 - \rho_2) g \int \langle h'^2 \rangle da. \tag{9.9}$$

The interaction kinetic energy K_I is, in general, not zero. This can be easily demonstrated in the case of the unstable hydrostatic Helmholtz wave which exists in this model when $f, d\bar{h}/dy, v_j'$ and $\partial/\partial y$ are put equal to zero. The same type of interaction energy also exists in the limiting case of pure shear instability (Section 4).

The sum of all five energy forms is constant, i.e.,

$$\frac{d}{dt}(K_M + P_M + K_I + K_E + P_E) = 0. \tag{9.10}$$

The equations are now to be interpreted in terms of our linearized small amplitude expansion (3.1). (We have an unstable wave in mind.) K_I, K_E and P_E are of order ϵ^2. We must therefore allow for changes in K_M and P_M of order ϵ^2. That is, we must consider the variation of $\langle \mathbf{v}_j \rangle$ and $\langle h \rangle$ to order ϵ^2. This requires a more detailed expansion of (3.1).

In order to avoid the use of additional subscripts to indicate orders of ϵ (subscripts already denoting layers 1 and 2), *we introduce the following special notation, which differs slightly from (9.4)*:

$$u_j = U_j + \epsilon u_j' + \epsilon^2 (U_j'' + X), \tag{9.11}$$

$$v_j = 0 + \epsilon v_j' + \epsilon^2 (V_j'' + X), \tag{9.12}$$

$$h = \bar{h} + \epsilon h' + \epsilon^2 (h'' + X), \tag{9.13}$$

$$w_1 = -h \nabla \cdot \mathbf{v}_1 = 0 + \epsilon w_1' + \epsilon^2 (w_1'' + X), \tag{9.14}$$

$$w_2 = (H - h) \nabla \cdot \mathbf{v}_2 = 0 + \epsilon w_2' + \epsilon^2 (w_2'' + X), \tag{9.15}$$

$$p_j = \bar{p}_j + \epsilon p_j' + \epsilon^2 (p_j'' + X). \tag{9.16}$$

In these equations $\bar{h}$, U_j and $\bar{p}_j$ are the parameters o Section 2 describing the basic unperturbed state, and are not functions of t. The terms u_j', v_j', h', p_j' now are the *first-order* perturbation quantities defined in (3.1), and no longer represent the total deviation from $\langle u_j \rangle$, etc. The terms w_1 and w_2 are the vertical velocities at the interface. The ϵ^2 terms have been divided into two parts—a part which is independent of x and denoted by U_j'', V_j'', h'', w_j'' and p_j'', and a part which varies with x but has a zero x average (formerly included in u_j', etc.). The latter part will not appear in the second-order x-averaged equations, and the symbol X is written in (9.11)–(9.16) merely to indicate that it is present in principle.

The procedure now is as follows. (A detailed derivation is given in Appendix B.) The notation of (9.11)–(9.16) is first introduced into the definitions (9.3)–(9.9) of the five energies, to order ϵ^2. The resulting expressions are differentiated with respect to t introducing various $\partial/\partial t$ terms in the five integrands. These $\partial/\partial t$ terms are then evaluated by substitution from the equations which result by substituting (9.11)–(9.16) into the original equations (2.2)–(2.4). The result is that the five time rates of change of the energies are each equal to certain energy transformation integrals W_m. Thus,

$$W_1 = \int \Big[\frac{d\bar{h}}{dy} (\rho_1 U_1 \langle u_1' v_1' \rangle - \rho_2 U_2 \langle u_2' v_2' \rangle) - (\rho_1 U_1 \langle u_1' w_1' \rangle - \rho_2 U_2 \langle u_2' w_2' \rangle) \Big] da, \tag{9.17}$$

$$W_2 = -f \int [\rho_1 U_1 \bar{h} V_1'' + \rho_2 U_2 (H - \bar{h}) V_2''] da, \tag{9.18}$$

$$W_3 = f \int [\rho_1 U_1 \langle h' v_1' \rangle - \rho_2 U_2 \langle h' v_2' \rangle] da, \tag{9.19}$$

$$W_4 = \int \Big[U_1 \Big\langle h' \frac{\partial p_1'}{\partial x} \Big\rangle - U_2 \Big\langle h' \frac{\partial p_2'}{\partial x} \Big\rangle \Big] da, \tag{9.20}$$

$$W_5 = -\int [\bar{h} \langle \mathbf{v}_1' \cdot \nabla p_1' \rangle + (H - \bar{h}) \langle \mathbf{v}_2' \cdot \nabla p_2' \rangle] da. \tag{9.21}$$

The time rates of change of the energies are:

$$\frac{1}{\epsilon^2} \frac{d}{dt} K_M = W_1 - W_2, \tag{9.22}$$

$$\frac{1}{\epsilon^2} \frac{d}{dt} P_M = W_2 - W_3, \tag{9.23}$$

$$\frac{1}{\epsilon^2} \frac{d}{dt} K_I = W_3 - W_4 - W_1, \tag{9.24}$$

$$\frac{1}{\epsilon^2} \frac{d}{dt} P_E = W_4 - W_5, \tag{9.25}$$

$$\frac{1}{\epsilon^2} \frac{d}{dt} K_E = W_5. \tag{9.26}$$

This energy flow is illustrated graphically in the upper part of Fig. 17. This diagram appears strange in that it is unsymmetric, with no energy flow between K_I and K_E. A more general arrangement is obtained by adding an arbitrary quantity A to W_1, W_2 and W_3 and any quantity B to W_4 and W_5, as shown in the bottom diagram of Fig. 17. [Note that this does not disturb the relations (9.22)–(9.26).] A more conventional diagram now results if we combine K_I and K_E and choose $A = 0$, $B = W_3 - W_4$. This is shown in Fig. 18. (This combination of K_I and K_E is not arbitrary, since they both arise from the same physical quantity—the kinetic energy integral.)

The physical meaning of W_1, W_2 and W_3 is (almost) clear. The integrand of W_1 has the general appearance of the Reynolds stress terms $-\langle u \rangle [\partial \langle u'v' \rangle / \partial y + \partial \langle u'w' \rangle / \partial z]$ which appear in a continuous model for

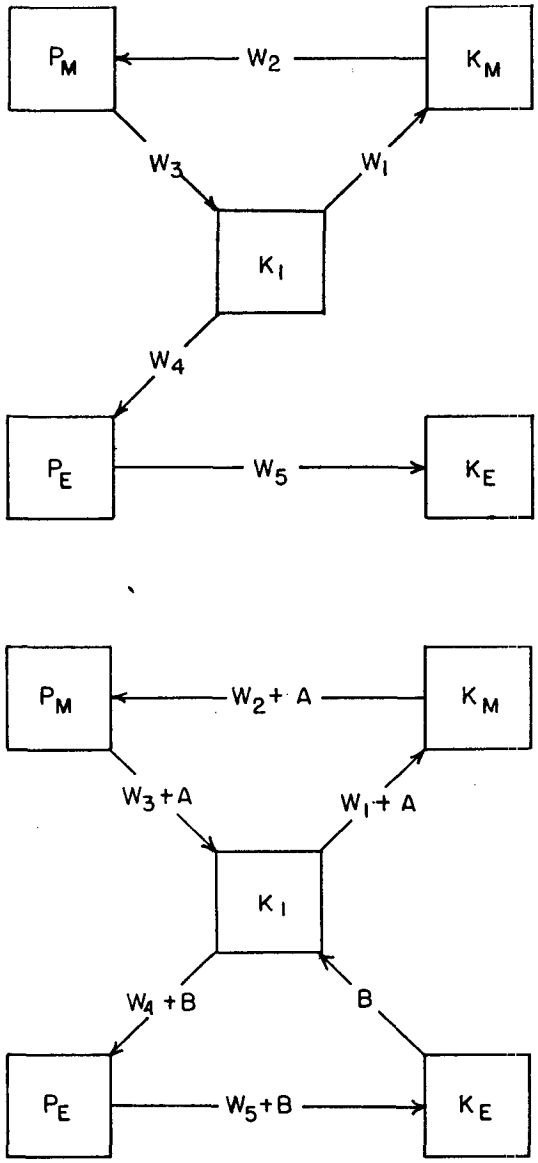

FIG. 17. Energy flow diagrams for the frontal model, in which K_E and K_I are kept distinct.

the transformation of eddy kinetic energy into mean kinetic energy. (The signs seem to be determined by the progression from layer 1 to 2 by proceeding in the positive z direction, but negative y direction.) It should be emphasized that both the $\langle u'v'\rangle$ and $\langle u'w'\rangle$ stresses are included in W_1. We can think of $\langle u'v'\rangle$ as typical of the shear instability waves of Section 2, and $\langle u'w'\rangle$ as typical of Helmholtz instability.

W_2 depends on the mean meridional circulation, V_j''. If $\bar{h}V_1''$ were the negative of $(H-\bar{h})V_2''$ (which it is not, in general), we could write the integrand as $\bar{h}V_1''f(\rho_2U_2-\rho_1U_1)=(\bar{h}V_1'')g(\rho_1-\rho_2)d\bar{h}/dy$. This could be transformed by partial integration with y into the integral of $-g(\rho_1-\rho_2)\bar{h}d(\bar{h}V_1'')/dy$. The y derivative in this expression can be thought of as a mean vertical velocity $\bar{w}$, say, giving the more familiar form of a correlation between $\bar{h}$ and $\bar{w}$.

W_3 can be given a heuristic interpretation by noting that if $\rho_1\sim\rho_2\sim\bar{\rho}$, and $U_2=-U_1=\bar{U}$, say, the integrand could be written as

$$-f\bar{\rho}\bar{U}\langle h'(v_1'+v_2')\rangle. \tag{9.27}$$

Let us take fU as positive, so that $d\bar{h}/dy$ is positive. Suppose h' is negatively correlated with $(v_1'+v_2')$. W_3 is then positive; the average of h'^2 must increase from this process. If particles moved strictly horizontally, with no divergence, they would carry with them their total value of h. The hypothesized negative correlation of h' with $(v_1'+v_2')$ would then mean that at places of positive h' particles on the average are arriving from higher latitudes bringing with them even larger h values; at places of negative h' particles on the average are arriving from lower latitudes bringing with them even smaller values of h. In this way, $\langle h'^2\rangle$ will increase. This process of increasing disturbance potential energy by horizontal advection processes is characteristic of the quasi-geostrophic baroclinic instability discovered by Charney (1947) and Eady (1949). It depends on the slope $d\bar{h}/dy$, which, in turn, is possible in the steady state only when f is present.

The sum $W_5+W_3-W_4$ does not have a clear kinematic interpretation yet because of the p' terms. In appendix B, however, it is shown that these combine to give

$$W_5+W_3-W_4 = \frac{f}{\tan\delta}\int[\rho_1U_1\langle w_1'h'\rangle-\rho_2U_2\langle w_2'h'\rangle]da. \tag{9.28}$$

Again choosing $U_2=-U_1=\bar{U}\approx\frac{1}{2}g(\rho_1-\rho_2)\tan\delta(f\bar{\rho})^{-1}$,

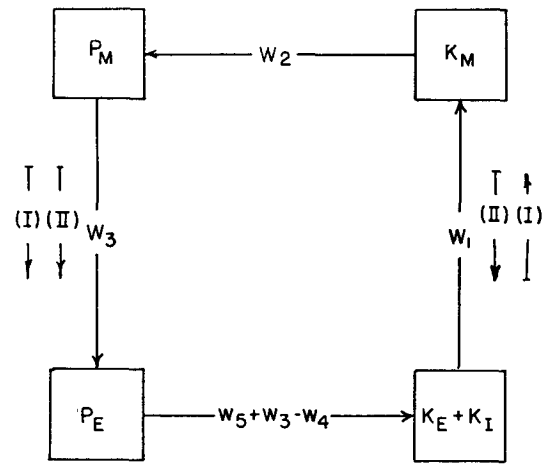

FIG. 18. Energy flow diagram for the frontal model combining K_E and K_I. The extra arrows indicate the direction of the transformations W_1 and W_3 in cases I and II.

this may be rewritten as

$$W_5+W_3-W_4 \approx -g(\rho_1-\rho_2)\int\left\langle\left(\frac{w_1'+w_2'}{2}\right)h'\right\rangle da. \quad (9.29)$$

P_E is therefore transformed into (K_I+K_E) by a correlation in x of descending motion with positive h', which decreases P_E by reducing the average magnitude of h'^2 and increases the magnitude of K_I+K_E by an equal amount.

I have computed numerically the energy transformation integrals W_1 and W_3 for the two cases I and II indicated on Fig. 9. Case I was described kinematically in Section 8. Case II also has Ri=5, but Ro=0.3, (a wavelength λ=2,090 km compared to λ=6,280 km for case I). As mentioned in the footnote following (8.1), Ro=0.3 has the largest growth rate for this value of Ri (at least for Ro<3), with a doubling time of 19.7 hr compared to the 32.5 hr of case I.

If W_3 is normalized to unity in both examples, the values of W_1 are

$$\left.\begin{array}{l}\text{Case I: } W_1=+0.07\\ \text{Case II: } W_1=-0.76\end{array}\right\}. \quad (9.30)$$

The more rapid growth rate of case II is evidently associated with a supply of energy to the growing perturbation from both potential and kinetic energy of the mean flow, whereas the more slowly developing case I waves returns to the mean kinetic energy some of the energy it receives from the mean potential energy. From the details of the numerical computation, it is apparent that the negative value of W_1 in case II vs its positive value in case I is due to the $\langle u'w'\rangle$ terms in W_1. Case II then partakes of geostrophic baroclinic instability *and* Helmholtz instability.

Although I have not made any further computations of W_1 and W_3, I believe they would show the following features:

1. Surface (H) corresponds to Helmholtz instability, with negative W_1 due to $\langle u'w'\rangle$.
2. Surface (E) is baroclinic instability with positive W_3 and negligible W_1.
3. At Ri<2, surface (R) has negative W_1 due to $\langle u'v'\rangle$, and is a barotropic (i.e., shear) instability of the Rayleigh type.
4. At Ri>2, surface (R) becomes more complicated. At very small Ro it retains feature 3, but as Ro increases and (R) and (E) approach one another, (R) also becomes baroclinic, with $W_3>0$. However, the growth rates are small on (R) as soon as Ri becomes appreciably greater than 2.
5. Surface (B), which occupies most of the range $0\leq$Ro≤ 1 when Ri is appreciably greater than 2, always has baroclinic instability ($W_3>0$). At small Ro it may have barotropic stability, as in case I above, but at larger Ro it will, as in case II, have barotropic instability as well, of the Helmholtz type.

Acknowledgments. I am deeply indebted to Prof. J. Charney for his suggestion of this problem, and for his constant interest, guidance and encouragement during the course of the investigation. I am also grateful for the time Profs. N. Phillips and J. Pedlosky spent with me in discussing the problem.

The numerical computations were made at the Computation Center of the Massachusetts Institute of Technology. It was supported by the National Science Foundation under contract G-18985 with the Massachusetts Institute of Technology.

APPENDIX A

The numerical method is an extension of the technique described by Fox (1959). I describe it for the general case, whose results are discussed in Section 7. The same technique was also used for the simpler cases of Ro=0 and τ=0 discussed in Sections 5 and 6. Consider a fixed value of the pair Ro, Ri. We set $\mathcal{P}_2(-1)=1$, and, formally, $\mathcal{P}_1(-1)=D$. The constants D and τ are unknown, as are the values of $\mathcal{P}_1(\eta)$ and $\mathcal{P}_2(\eta)$ for $-1\leq\eta\leq 1$. Eqs. (5.3) and (5.4) are, symbolically

$$\mathfrak{M}_1(\mathcal{P}_1,\mathcal{P}_2;\tau)=0, \quad (A.1)$$

$$\mathfrak{M}_2(\mathcal{P}_1,\mathcal{P}_2;\tau)=0, \quad (A.2)$$

where $\mathfrak{M}_1$ and $\mathfrak{M}_2$ are second order differential operators. At $\eta=-1$ we have (7.4) and (5.5), i.e.,

$$\left(\frac{d\mathcal{P}_1}{d\eta}\right)_{\eta=-1}=\mathrm{Ri}\left[\frac{1}{\tau-1}+\frac{1-\mathrm{Ro}^2(\tau-1)^2}{2}\right]D - \frac{\mathrm{Ri}}{2}[1-\mathrm{Ro}^2(\tau-1)^2], \quad (A.3)$$

$$\left(\frac{d\mathcal{P}_2}{d\eta}\right)_{\eta=-1}=\mathrm{RiRo}. \quad (A.4)$$

At $\eta=+1$ we have (7.5) and (5.5). These we choose to write as

$$F=\left\{\frac{d\mathcal{P}_1}{d\eta}+\mathrm{RiRo}\mathcal{P}_1\right\}_{\eta=1}=0, \quad (A.5)$$

$$G=\left\{\frac{d\mathcal{P}_2}{d\eta}-\frac{\mathrm{Ri}}{\tau+1}\mathcal{P}_2 - \frac{\mathrm{Ri}}{2}[1-\mathrm{Ro}^2(\tau+1)^2](\mathcal{P}_1-\mathcal{P}_2)\right\}_{\eta=1}=0. \quad (A.6)$$

The interval from $\eta=-1$ to $\eta=+1$ is divided into 40 intervals and $d\mathcal{P}/d\eta$ and $d^2\mathcal{P}/d\eta^2$ are expressed in finite differences where they appear in (A.1)–(A.6). $\mathcal{P}_1$ and $\mathcal{P}_2$

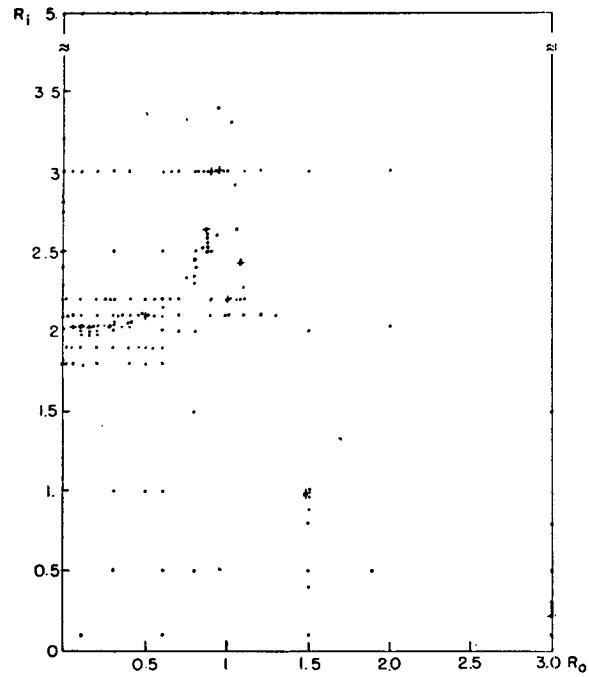

FIG. 19 Location of all Ri-Ro points for which the computations were made.

could then be computed at successive discrete η values, $\eta=-0.95, -0.90, \ldots$, up to $\eta=+1$, for a pair of trial values τ_ν, D_ν. The values of $\mathcal{P}_j$ at $\eta=1$ so obtained will not satisfy (A.5)–(A.6), in general, and a revised guess must therefore be made for τ and D.

A logical way to correct τ and D is as follows. Let the numerical solution be viewed (for fixed Ro, Ri), as a function of τ and D. Introduce $\mathcal{S}_j$ and $\mathcal{T}_j$ for the differential coefficients

$$\mathcal{S}_j=\frac{\partial \mathcal{P}_j}{\partial \tau}; \quad \mathcal{T}_j=\frac{\partial \mathcal{P}_j}{\partial D}. \tag{A.7}$$

Partial differentiation of (A.1)–(A.2) with respect to τ and D produces four new second order differential equations of the form

$$\mathfrak{M}_1(\mathcal{T}_1,\mathcal{T}_2;\tau)=0, \tag{A.8}$$

$$\mathfrak{M}_2(\mathcal{T}_1,\mathcal{T}_2;\tau)=0, \tag{A.9}$$

$$\mathfrak{M}_1(\mathcal{S}_1,\mathcal{S}_2;\tau)=\mathfrak{N}_1(\mathcal{P}_1,\mathcal{P}_2;\tau), \tag{A.10}$$

$$\mathfrak{M}_2(\mathcal{S}_1,\mathcal{S}_2;\tau)=\mathfrak{N}_2(\mathcal{P}_2,\mathcal{P}_2;\tau). \tag{A.11}$$

$\mathfrak{M}_1$ and $\mathfrak{M}_2$ are the second-order differential operators appearing in (A.1) and (A.2). $\mathfrak{N}_1$ and $\mathfrak{N}_2$ are the first-order differential operators which appear when the coefficients in $\mathfrak{M}_1$ and $\mathfrak{M}_2$ are differentiated with respect to τ. A similar treatment is given the four boundary conditions (A.3)–(A.6).

Step-wise integration from $\eta=-1$ can now be performed simultaneously for $\mathcal{P}_j$, $\mathcal{S}_j$, and $\mathcal{T}_j$. F and G will not be zero, but will equal F_ν, and G_ν, say, when $\eta=1$ is reached. We obtain a correction to the guessed constants τ and D by using Newton's method of finding roots. This amounts to solving the simultaneous set of (complex) equations

$$\left(\frac{\partial F}{\partial \tau}\right)\Delta\tau+\left(\frac{\partial F}{\partial D}\right)\Delta D=-F_\nu, \tag{A.12}$$

$$\left(\frac{\partial G}{\partial \tau}\right)\Delta\tau+\left(\frac{\partial G}{\partial D}\right)\Delta D=-G_\nu, \tag{A.13}$$

for $\Delta\tau$ and ΔD. [The differential coefficients here are the expressions involving $\mathcal{P}_j$, $\mathcal{S}_j$ and $\mathcal{T}_j$ obtained when (A.5) and (A.6) were differentiated with respect to τ and D.] The process is then repeated (for the same Ro, Ri pair) with $\tau_{\nu+1}=\tau_\nu+\Delta\tau$ and $D_{\nu+1}=D_\nu+\Delta D$, until satisfactory convergence is obtained. I used the criterion that $|\Delta\tau|$ and $|\Delta D|$ must be less than 10^{-5}.

I also made several tests with 200 intervals between $\eta=\pm1$. The results differed insignificantly from the 40-interval results for the smoothly varying $\mathcal{P}_j(\eta)$ associated with the particular values of Ro and Ri I have investigated.

The convergence was more rapid in τ than in D. A more flexible system, in which $\mathcal{P}_2(-1)$ is allowed to vary instead of being fixed at 1, might have better convergence. Most of the τ values were obtained by using as initial guesses for τ and D numerical values previously obtained at neighboring Ro-Ri values. This procedure was unsatisfactory in the vicinity of point where $\tau=0$, because $D=\mathcal{P}_1(\eta=-1)\div\mathcal{P}_2(\eta=-1)$ passes through infinity there (Kotschin, 1932).

The location of all possible τ values (for fixed Ro, Ri) by this method is not guaranteed, although by using a wide range of initial guesses, as I have done, considerable confidence can be placed on the numerical results.

Fig. 19 shows the location of all Ri-Ro points for which these computations were made. Appendix C lists the τ values.

APPENDIX B

The energies defined in (9.5)–(9.9) are of order ϵ^0 and ϵ^2, plus higher order terms. The zero order terms are constant, according to (9.11)–(9.16). Differentiating with respect to t, and introducing the special notation of (9.11)–(9.16), we have, for the ϵ^2 contribution,

$$\frac{1}{\epsilon^2}\frac{dK_M}{dt}=\int\rho_1\left[\bar{h}U_1\frac{\partial U_1''}{\partial t}+\frac{U_1^2}{2}\frac{\partial h''}{\partial t}\right]$$

$$+\rho_2\left[(H-\bar{h})U_2\frac{\partial U_2''}{\partial t}-\frac{U_2^2}{2}\frac{\partial h''}{\partial t}\right]da, \tag{B.1}$$

$$\frac{1}{\epsilon^2}\frac{dP_M}{dt}=g(\rho_1-\rho_2)\int \bar{h}\frac{\partial h''}{\partial t}da, \tag{B.2}$$

$$\frac{1}{\epsilon^2}\frac{dK_I}{dt}=\int\left[\rho_1 U_1\frac{\partial}{\partial t}\langle u_1'h'\rangle-\rho_2 U_2\frac{\partial}{\partial t}\langle u_2'h'\rangle\right]da, \tag{B.3}$$

$$\frac{1}{\epsilon^2}\frac{dK_E}{dt}=\int\left[\rho_1\bar{h}\left\langle \mathbf{v}_1'\cdot\frac{\partial \mathbf{v}_1'}{\partial t}\right\rangle +\rho_2(H-\bar{h})\left\langle \mathbf{v}_2'\cdot\frac{\partial \mathbf{v}_2'}{\partial t}\right\rangle\right]da, \tag{B.4}$$

$$\frac{1}{\epsilon^2}\frac{dP_E}{dt}=g(\rho_1-\rho_2)\int\left\langle h'\frac{\partial h'}{\partial t}\right\rangle da. \tag{B.5}$$

The original equations (2.2)–(2.4) to first order in ϵ are

$$\left[\frac{\partial}{\partial t}+U_j\frac{\partial}{\partial x}+f\mathbf{k}X\right]\mathbf{v}_j'=-\frac{1}{\rho_j}\nabla p_j', \tag{B.6}$$

$$p_1'=p_2'+(\rho_1-\rho_2)gh', \tag{B.7}$$

$$\frac{\partial h'}{\partial t}=-\left[U_1\frac{\partial h'}{\partial x}+v_1'\frac{d\bar{h}}{dy}\right]-\bar{h}\nabla\cdot\mathbf{v}_1' =-\left[U_1\frac{\partial h'}{\partial x}+v_1'\frac{d\bar{h}}{dy}\right]+w_1', \tag{B.8}$$

$$\frac{\partial h'}{\partial t}=-\left[U_2\frac{\partial h'}{\partial x}+v_2'\frac{d\bar{h}}{dy}\right]+(H-\bar{h})\nabla\cdot\mathbf{v}_2' =-\left[U_2\frac{\partial h'}{\partial x}+v_2'\frac{d\bar{h}}{dy}\right]+w_2'. \tag{B.9}$$

To second order in ϵ, the x-averaged equations [again in the special notation of (9.11)–(9.16)] are

$$\frac{\partial U_j''}{\partial t}=-\frac{\partial\langle u_j'v_j'\rangle}{\partial y}+\langle u_j'\nabla\cdot\mathbf{v}_j'\rangle+fV_j'', \tag{B.10}$$

$$\frac{\partial V_j''}{\partial t}=-\frac{\partial}{\partial y}\langle v_j'v_j'\rangle+\langle v_j'\nabla\cdot\mathbf{v}_j'\rangle-fU_j''-\frac{1}{\rho_j}\frac{\partial p_j''}{\partial y}, \tag{B.11}$$

$$\frac{\partial h''}{\partial t}=-\frac{\partial}{\partial y}[\bar{h}V_1''+\langle h'v_1^1\rangle] =\frac{\partial}{\partial y}[(H-h)V_2''-\langle h'v_2'\rangle]. \tag{B.12}$$

Eq. (B.11) is included only for completeness, since $\partial V_j''/\partial t$ does not appear in (B.1). The following expressions result from obvious manipulation of (B.6)–(B.9):

$$\left\langle \mathbf{v}_j'\cdot\frac{\partial \mathbf{v}_j'}{\partial t}\right\rangle=-\frac{1}{\rho_j}\langle \mathbf{v}_j'\cdot\nabla p_j'\rangle, \tag{B.13}$$

$$\frac{\partial}{\partial t}\langle u_j'h'\rangle=f\langle v_j'h'\rangle-\frac{1}{\rho_j}\left\langle h'\frac{\partial p_j'}{\partial x}\right\rangle -\langle u_j'v_j'\rangle\frac{d\bar{h}}{dy}+\langle u_j'w_j'\rangle. \tag{B.14}$$

These are now introduced into (B.1)–(B.3) to eliminate the time derivatives.

To derive (9.22) we substitute (B.10) and (B.12) into (B.1). Thus,

$$\frac{1}{\epsilon^2}\frac{dK_M}{dt}=\int\rho_1\left\{\bar{h}U_1\left[fV_1''+\langle u_1'\nabla\cdot\mathbf{v}_1'\rangle -\frac{\partial}{\partial y}\langle u_1'v_1'\rangle\right]-\frac{U_1^2}{2}\frac{\partial}{\partial y}[V_1''\bar{h}+\langle h'v_1'\rangle]\right\} +\rho_2\left\{(H-\bar{h})U_2\left[fV_2''+\langle u_2'\nabla\cdot\mathbf{v}_2'\rangle-\frac{\partial}{\partial y}\langle u_2'v_2'\rangle\right] -\frac{U^2}{2}\frac{\partial}{\partial y}[V_2''(H-\bar{h})-\langle h'v_2'\rangle]\right\}da. \tag{B.15}$$

The two Coriolis terms give $-W_2$ according to the definition (9.18). At this point, we specialize to the frontal model, in which U_1 and U_2 are independent of y. The U_j^2 terms then vanish in the y integration. From (9.14) and (9.15) we have

$$w_1'=-\bar{h}\nabla\cdot\mathbf{v}_1', \tag{B.16}$$

$$w_2'=(H-\bar{h})\nabla\cdot\mathbf{v}_2'. \tag{B.17}$$

Thus,

$$\frac{1}{\epsilon^2}\frac{dK_M}{dt}=-W_2+\int\rho_1U_1\left[-\langle u_1'w_1'\rangle-\bar{h}\frac{\partial}{\partial y}\langle u_1'v_1'\rangle\right] +\rho_2U_2\left[\langle u_2'w_2'\rangle+(H-\bar{h})\frac{\partial}{\partial y}\langle u'^2v_2'\rangle\right]da =-W_2+W_1, \tag{B.18}$$

the last step being based on partial integration of the $\partial\langle u_j'v_j'\rangle/\partial y$ terms.

To derive (9.23) we first substitute (B.12) into (B.2) to obtain

$$\frac{1}{\epsilon^2}\frac{dP_M}{dt}=-g\int\bar{h}\frac{\partial}{\partial y}\{\rho_1[\bar{h}V_1''+\langle h'v_1'\rangle]+\rho_2[(H-\bar{h})V_2''-\langle h'v_2'\rangle]\}da. \quad \text{(B.19)}$$

Now, from (B.12), with the boundary conditions that V_j'' and v_j' vanish at $|y|=\infty$, we have

$$\bar{h}V_1''+\langle h'v_1'\rangle=(H-\bar{h})V_2''-\langle h'v_2'\rangle. \quad \text{(B.20)}$$

Eq. (B.19) is integrated by parts with respect to y, $d\bar{h}/dy$ is replaced by (2.5), and then free use is made of (B.20). The result is

$$\frac{1}{\epsilon^2}\frac{dP_M}{dt}=-f\int\{\rho_1U_1[\bar{h}V_1''+\langle h'v_1'\rangle]+\rho_2U_2[(H-\bar{h})V_2''-\langle h'v_2'\rangle]\}da=W_2-W_3. \quad \text{(B.21)}$$

The derivation of (9.26) from (B.3) and (B.13) is trivial, as is the derivation of (9.24) from (B.4) and (B.14). The truth of (9.25) is established by inserting (9.20) and (9.21) into (9.25) and using (B.8) and (B.9). Thus,

$$W_4-W_5=\int\left[U_1\left\langle h'\frac{\partial p_1'}{\partial x}\right\rangle+\bar{h}\langle\mathbf{v}_1'\cdot\nabla p_1'\rangle\right]-\left[U_2\left\langle h'\frac{\partial p_2'}{\partial x}\right\rangle-(H-\bar{h})\langle\mathbf{v}_2'\cdot\nabla p_2'\rangle\right]da. \quad \text{(B.22)}$$

The $\langle\mathbf{v}_j'\cdot\nabla P_j'\rangle$ terms are transformed into $\langle\nabla\cdot p_j'\mathbf{v}_j'\rangle-\langle p_j'\nabla\cdot\mathbf{v}_j'\rangle$ and the $\nabla\cdot\mathbf{v}_j'$ terms are replaced from the left hand parts of (B.8) and (B.9). The integrand in (B.22) becomes

$$U_1\left\langle\frac{\partial}{\partial x}(p_1'h')\right\rangle+\frac{\partial}{\partial x}[\langle p_1'v_1'\rangle\bar{h}]-U_2\left\langle\frac{\partial}{\partial x}(p_2'h')\right\rangle+\frac{\partial}{\partial y}[\langle p_2'v_2'\rangle(H-\bar{h})]+\left\langle(p_1'-p_2')\frac{\partial h'}{\partial t}\right\rangle.$$

The first four terms vanish on integration. From (B.7) we then obtain

$$W_4-W_5=(\rho_1-\rho_2)g\int\left\langle h'\frac{\partial h'}{\partial t}\right\rangle da=\frac{1}{\epsilon^2}\frac{dP_E}{dt}. \quad \text{(B.23)}$$

The proof of the critical equality (9.28) amounts to establishing that

$$(\rho_1-\rho_2)g\tan\delta\int\left\langle h'\frac{\partial h'}{\partial t}\right\rangle da=-f\int[\rho_1U_1\langle w_1'h'\rangle-\rho_2U_2\langle w_2'h'\rangle]da+f\tan\delta\int[\rho_1U_1\langle v_1'h'\rangle-\rho_2U_2\langle v_2'h'\rangle\ da.$$

The validity of this follows from the right parts of (B.8) and (B.9) and the relation (2.5) for $\tan\delta$.

APPENDIX C

Ri	Ro	$\lvert\tau_r\rvert$	$\lvert\tau_i\rvert$
0.1	0.1	—	0.9968
0.1	0.6	—	0.9943
0.1	1.5	—	0.9557
0.1	3.0	—	0.8242
0.2	3.0	—	0.4676
0.21	3.0	—	0.2790
0.22	3.0	—	0.2947
0.22	3.0	0.4606	—
0.2205	3.0	0.4550	—
0.235	3.0	0.2646	0.1153
0.24	3.0	0.3326	0.2421
0.25	3.0	0.3645	0.2903
0.3	3.0	0.4281	0.3739
0.4	1.5	—	0.6721
0.5	0.3	—	0.9569
0.5	0.6	—	0.8968
0.5	0.8	—	0.8414
0.5	0.95	—	0.7925
0.5	1.5	—	0.5726
0.5	1.9	—	0.3229
0.5	3.0	0.4648	0.3344
0.8	1.5	—	0.2588
0.8	3.0	0.6604	—
0.9	1.5	—	0.1643
0.98	1.5	—	0.0465
0.99	1.48	0.0394	0.0465
0.99	1.5	0.0999	—
1.00	0.3	—	0.7570
1.00	0.6	—	0.7050
1.00	1.5	0.3261	—
1.5	0.8	—	0.3627
1.5	3.0	0.4274	—
1.8	0.001	—	0.9550
1.8	0.01	—	0.9478
1.8	0.01	0.2131	—
1.8	0.05	—	0.9071
1.8	0.2	—	0.7450
1.8	0.2	0.2643	—
1.8	0.4	0.3575	—

Ri	Ro	$\lvert\tau_r\rvert$	$\lvert\tau_i\rvert$
1.8	0.6	—	0.3525
1.8	0.6	0.4896	—
1.9	0.01	0.1450	—
1.9	0.05	—	0.9210
1.9	0.1	—	0.8613
1.9	0.2	—	0.7359
1.9	0.3	—	0.6056
1.9	0.4	—	0.4792
1.9	0.45	—	0.4225
1.9	0.5	—	0.3730
1.9	0.55	—	0.3315
1.9	0.6	—	0.2975
1.98	0.1	—	0.8511
1.98	0.15	—	0.7839
1.98	0.2	—	0.7143
1.99	0.1	—	0.8497
1.99	0.15	—	0.7819
1.95	0.15	—	0.7809
2.00	0.1	—	0.8484
2.00	0.15	—	0.7798
2.00	0.2	—	0.8086
2.00	0.3	—	0.5594
2.00	0.6	—	0.2339
2.00	0.6	0.4542	—
2.00	0.7	—	0.1992
2.00	0.8	0.2352	—
2.00	1.5	0.3054	—
2.01	0.01	—	0.9415
2.01	0.01	—	0.0456
2.01	0.1	—	0.8471
2.02	0.001	—	0.0657
2.02	0.05	—	0.0800
2.02	0.07	—	0.0806
2.02	0.1	—	0.0805
2.02	0.15	—	0.0776
2.02	0.15	—	0.7567
2.02	0.18	—	0.0730
2.03	0.05	—	0.0854
2.03	0.1	—	0.0862
2.03	0.15	—	0.0833
2.03	0.15	—	0.0807
2.03	0.19	—	0.0769
2.03	0.20	—	0.6998
2.03	0.21	—	0.0715
2.03	0.24	—	0.0588
2.03	0.27	—	0.0327
2.03	0.28	—	0.0085
2.03	0.30	—	0.5429
2.03	0.35	—	0.4610
2.03	0.40	—	0.3807
2.03	2.00	0.4786	—
2.04	0.4	—	0.3694
2.05	0.3	—	0.5311
2.05	0.4	—	0.4440
2.05	0.4	—	0.3566
2.1	0.01	—	0.1418
2.1	0.02	—	0.1481
2.1	0.05	—	0.1587
2.1	0.05	—	0.8843
2.1	0.1	—	0.8454
2.1	0.1	—	0.1672
2.1	0.2	—	0.6778
2.1	0.2	—	0.1751
2.1	0.3	—	0.4963
2.1	0.3	—	0.1911
2.1	0.32	0.0001	0.2224
2.1	0.35	0.0004	0.2596
2.1	0.40	0.0669	0.2381
2.1	0.45	0.1493	0.1829
2.1	0.48	0.0050	0.0586
2.1	0.5	0.1702	0.0757
2.1	0.51	—	0.1294
2.1	0.55	—	0.1446
2.1	0.55	0.3625	—
2.1	0.6	0.6629	—
2.1	0.7	—	0.1106
2.1	0.7	0.4107	—
2.1	0.9	—	0.0703
2.1	0.9	0.0888	—
2.1	0.99	—	0.0272
2.1	1.05	—	0.0259
2.1	1.1	0.0488	0.0510
2.1	1.2	0.1215	0.0401
2.1	1.3	0.1780	0.1089
2.2	0.1	—	0.8202
2.2	0.1	—	0.2282
2.2	0.2	—	0.6204
2.2	0.2	—	0.2756
2.2	0.25	—	0.5035
2.2	0.25	—	0.2191
2.2	0.28	0.0553	0.3883
2.2	0.3	0.1014	0.3725
2.2	0.4	0.1917	0.2841
2.2	0.5	0.2504	0.1769
2.2	0.55	0.2655	0.0929
2.2	0.6	0.1678	—
2.2	0.65	0.4203	—
2.2	0.70	0.3535	—
2.2	.9	—	0.1091
2.2	1.0	—	0.1117
2.2	1.05	—	0.0810
2.2	1.06	0.0135	0.0611
2.2	1.08	0.0388	0.0579
2.2	1.10	0.0566	0.0554
2.3	0.8	0.1356	0.0763
2.35	0.8	0.1426	0.0843
2.40	0.8	0.1479	0.0903
2.45	0.8	0.1521	0.0951
2.50	0.8	0.1554	0.0991
2.50	0.87	0.0795	0.0253
2.50	0.90	0.0528	0.0490
2.53	0.87	0.0761	0.0311
2.55	0.87	0.0848	0.0349
2.59	0.87	0.0880	0.0396
2.60	0.87	0.0887	0.0406
2.60	0.94	0.0283	0.0667
2.61	0.87	0.0893	0.0415
2.62	0.87	0.0899	0.0423
2.63	0.87	0.0905	0.0431
3.00	0.001	—	0.3987
3.00	0.01	—	0.4071
3.00	0.05	—	0.4568
3.00	0.1	0.0612	0.5979
3.00	0.2	0.2566	0.5054
3.00	0.3	0.3227	0.4256
3.00	0.4	0.3582	0.3313
3.00	0.6	0.3788	0.0676
3.00	0.65	0.5549	—
3.00	0.65	0.3556	0.0593
3.00	0.70	0.3995	—
3.00	0.80	0.1892	—
3.00	0.82	0.1497	0.0323
3.00	0.85	0.1195	0.0518
3.00	0.88	0.0912	0.0631
3.00	0.89	0.0823	0.0658
3.00	0.90	0.0735	0.0682
3.00	0.92	0.0565	0.0721
3.00	0.94	0.0401	0.0749
3.00	0.95	0.0319	0.0671
3.00	1.0	—	0.0891
3.00	1.1	0.0675	0.0772
3.00	1.2	0.1231	0.0704
3.00	1.5	0.2475	0.0240
5.00	0.1	0.3028	0.5957
5.00	0.3	0.4344	0.3626
5.00	0.4	0.4389	0.2466
5.00	0.5	0.4225	0.1132
5.00	0.9	0.0714	0.1171
5.00	1.0	0.0560	0.1280
5.00	1.1	0.0697	0.1308
5.00	1.2	0.1242	0.1298
5.00	1.3	0.1711	0.1271

REFERENCES

Bjerknes, J., 1919: On the structure of moving cyclones. *Geofys. Publikasjoner*, **1**, No. 2.

——, and C. Godske, 1936: On the theory of cyclone formation at extra-tropical fronts. *Astrophys. Norv.*, **1**, No. 6, 199–235.

Charney, J. G., 1947: The dynamics of long waves in a baroclinic westerly current. *J Meteor.*, **4**, 135–162.

——, 1951: On baroclinic instability and the maintenance of the kinetic energy of the westerlies. Union Geodesique et Geophys. Intern., Bruxelle, 47–63.

Eady, E., 1949: Long waves and cyclonic waves. *Tellus*, **1**, No. 3, 33–52.

Eliasen, E., 1960: On the initial development of frontal waves. *Pub. Det. Danske Meteor. Inst.*, No. 13, 107 pp.

Fjørtoft, R., 1951: Some results concerning the distribution and total amount of kinetic energy in the atmosphere. *The Atomosphere and Sea in Motion*, New York, Rockefeller Institute and Oxford University Press, 509 pp.

Fox, L., 1959: Some numerical experiments with eigenvalue problems in ordinary differential equations. *Boundary Problems in Differential Equations*, The University of Wisconsin Press, 324 pp.

Fultz, D., 1952: On the possibility of experimental models of the polar front. *J. Meteor.*, **9**, 379–384.

Haurwitz, B., and H. Panofsky, 1950: Stability and meandering of the Gulf Stream. *Trans. Amer. Geophys. Union*, **31**, 723–731.

Høiland, E., 1948: Stability and instability waves in sliding layers with internal static stability. *Arch. Math. Naturvidensk.*, **50**, No. 3.

Kotschin, N., 1932: Über die Stabilität von Margulesschen Diskontinuitätsflächen. *Beitr. Phys. Atmos.*, **18**, 129–164.

Lamb, H., 1932: *Hydrodynamics*. Dover, New York, 738 pp.

Pedlosky, J., 1964: The stability of currents in the atmosphere and the ocean. *J. Atmos. Sci.*, **21**, 201–219.

Phillips, N., 1954: Energy transformations and meridional circulations associated with sample baroclinic waves in a two-layer model. *Tellus*, **6**, 273–280.

——, 1963: Geostrophic motion. *Rev. Geophys.*, **1**, 123–176.

Rayleigh, Lord, 1879: On the stability of jets. *Proc. London Math. Soc.*, **10**, 4–13.

Solberg, H., 1928: Integrationen der atmosphärischen Störungsgleichungen. *Geofys. Publikasjoner*, **5**, No. 9.

Stone, P., 1966: On non-geostrophic baroclinic stability. *J. Atmos. Sci.*, **23**, 390–400.